

Revealing the dust grain polarization properties as a function of extinction and distance towards NGC 1893

N. Bijas,^{1*} Chakali Eswaraiah,^{1†} Jia-Wei Wang,² Jessy Jose,¹ Wen-Ping Chen,³ Di Li,^{4,5} Shih-Ping Lai,⁶ D. K. Ojha⁷

¹Indian Institute of Science Education and Research (IISER) Tirupati, Rami Reddy Nagar, Karakambadi Road, Mangalam (P.O.), Tirupati 517 507, India

²Academia Sinica Institute of Astronomy and Astrophysics, No. 1, Section 4, Roosevelt Road, Taipei 10617, Taiwan

³Graduate Institute of Astronomy, National Central University, Zhongli, Taoyuan 32001, Taiwan

⁴CAS Key Laboratory of FAST, National Astronomical Observatories, Chinese Academy of Sciences, Peoples Republic of China

⁵University of Chinese Academy of Sciences, Beijing 100049, People's Republic of China

⁶Institute of Astronomy, National Tsing Hua University, No. 101, Section 2, Kuang-Fu Road, Hsinchu 30013, Taiwan

⁷Department of Astronomy and Astrophysics, Tata Institute of Fundamental Research, Homi Bhabha Road, Mumbai 400 005, India

Accepted 2022 July 5. Received 2022 July 5; in original form 2022 May 6

ABSTRACT

Dust polarization observations at optical wavelengths help to understand the dust grain properties and trace the plane-of-the-sky component of the magnetic field. In this study, we make use of the *I*-band polarization data acquired from AIMPOL along with the distances (d) and extinction (A_V) data to study the variation of polarization fraction (P) as a function of A_V and d towards the star-forming region, NGC 1893. We employ a broken power-law fit and Bayesian analysis on extinction (A_V) versus polarization efficiency (P/A_V) and distance (d) versus rate of polarization (P/d). We find that P/A_V shows a break at an extinction of ~ 0.9 mag, whereas P/d exhibits a break at a distance of ~ 1.5 kpc. Based on these, we categorize the dust towards NGC 1893 into two populations: (i) foreground dust confined to $A_V < \sim 1$ mag and distance up to ~ 2 kpc and (ii) Perseus spiral arm dust towards NGC 1893 characterized with $A_V > \sim 1$ mag and distance beyond ~ 2 kpc. Foreground dust exhibits higher polarization efficiency but a lower polarization rate, whereas Perseus dust shows a lower polarization efficiency but a slightly higher polarization rate. Hence, we suggest that while polarization efficiency reveals the dust grain alignment, the rate of polarization infers about the distribution of dust grains towards NGC 1893. Further, we also shed a light on the spatial variation of intrinsic polarization and magnetic field orientation, and other parameters within the intra-cluster medium of NGC 1893.

Key words: polarization, dust, extinction, magnetic fields

1 INTRODUCTION

Interstellar dust polarization has been studied extensively for more than half a century since it was observed for the first time at visible wavelengths by Hall (1949) and Hiltner (1949a). It has been proposed that the observed polarization was caused by the dichroic extinction of asymmetrical dust grains, which are aligned with respect to the Galactic magnetic field (Hiltner 1949b; Davis Jr & Greenstein 1951).

Since magnetic alignment of the dust grains is a prerequisite for the interstellar polarization to occur, several mechanisms have been proposed to explain it (see, Andersson et al. 2015). Nevertheless, most of the theoretical and experimental evidence points towards the radiative alignment torque (RAT) mechanism as the most probable mechanism for dust grain alignment, which can then explain

the observed optical/NIR and far-infrared/millimeter polarization in the interstellar medium (Lazarian 2007; Lazarian & Hoang 2007; Andersson et al. 2011). According to the RAT mechanism, when the radiation incidents upon an irregular dust grain, there is a difference in the extinction cross-sections experienced by the left circular and right circular polarization components of the incident light. This results in the generation of radiative torques which act on the grains, causing them to spin up due to increased angular momentum. In the presence of an external magnetic field, the grains Larmor precesses around the magnetic field, and the radiative torques acting over the precessing period align the grains with the field (Dolginov & Mytrophanov 1976; Draine & Weingartner 1996; Draine & Weingartner 1997).

When the background starlight passes through these magnetically aligned dust grains, its electric vector parallel to the long axis of the dust grains encounter a maximum extinction cross-section as compared to that parallel to the short axis. This differential extinction cross-section causes the transmitted starlight through the dust grains to be partially plane-polarized up to a few percent. The observed polarized light yield, two important parameters – (i) fraction of

* Email: bijas@iiser.ac.in, bijasn@students.iiser.ac.in

† Ramanujan Fellow; Email: eswaraiah@labs.iiser.ac.in

polarization (P), which reveals the averaged dust grain properties along the line of sight (LOS), and (ii) polarization angle (PA), which reveals the LOS averaged magnetic field projected on the plane of the sky (POS) (Davis Jr & Greenstein 1951; Lazarian & Hoang 2007).

It has been observed that in optical V -band, the observed polarization, P , increases with total extinction (A_V), and the distribution for various lines of sight suggest, an upper limit of $P/A_V < 3\%$ mag^{-1} (Serkowski et al. 1975). A key conclusion from these data is that P does not increase in the same proportion as A_V does, owing to several factors that include (i) the properties of dust grains themselves such as the grain size (e.g., $\sim 0.1 - 0.3 \mu\text{m}$), shape (e.g. oblate or prolate), composition (e.g. silicate, graphite or graphite-silicate), mantle to core volume ratio, presence or absence of surface coatings, (ii) magnetic field orientation weighted according to the distribution of dust grains along the line of sight, (iii) the efficiency of grain alignment, and (iv) inclination angle between the actual magnetic field with respect to LOS, and (v) the physical conditions of the environment in which dust exist (see Lee & Draine 1985). Therefore, observed polarization measurements need to be critically analysed before interpreting the data.

One of the key concerns is to know whether the polarization measurements of a distant target would reveal the dust grain properties and magnetic field orientation of foreground dust only, but not of intra-cluster medium of a distant cluster, or all the dust grains along the line of sight to the target. To be specific about what regime of A_V is responsible for the observed polarization observations, one of the promising approaches would be analysing the variation of the ratio P/A_V , the dust grain polarization efficiency, as a function of A_V , e.g. by means of a power-law fit of the form $P/A_V \propto A_V^{-\alpha}$. The power-law index α at different ranges of A_V hints at dust grain alignment efficiency at those corresponding layers of dust. For example, $\alpha = 1$ corresponds to the total loss of dust grain alignment, and $\alpha = 0$ corresponds to the efficiently aligned dust grains at all optical depths (e.g. Pattle et al. 2019). These interpretations are similar to those based on the index α in the relation $P' \propto I'^{-\alpha}$, where P' and I' are the dust emission polarization and intensity, respectively at sub-millimeter wavelength (e.g. Jones et al. 2015; Wang et al. 2019; Pattle et al. 2019). The study of polarization efficiency at various wavelengths has been the subject of research (Goodman et al. 1992, 1995; Gerakines et al. 1995; Andersson & Potter 2005; Franco et al. 2010; Wang et al. 2017). The majority of these studies have shown that P/A_V varies as a function of A_V with the α values ranging from about -1 to -0.5 .

In this work, we examine the relation between A_V versus P/A_V towards the direction of a prominent star forming region NGC 1893, located at a distance of 3.2 kpc (Kharchenko et al. 2005), with an average age of 2–3 Myr (Massey et al. 1995). NGC 1893 is an active star forming region hosting young massive O/B type stars and two elephant trunk-like nebulae Sim 129 and 130 shown in Figure 1. Therefore, it is an interesting region to study the dust properties and magnetic field orientations influencing star formation and polarization. This region has been investigated extensively over several years (Gaze & Shajn 1952; Massey et al. 1995; Marco & Negueruela 2002; Maheswar et al. 2007; Sharma et al. 2007) and has existing polarization data (Eswaraiah et al. 2011).

Another critical parameter that can be used to study the dust properties is the ratio of polarization to distance, P/d , as a function of distance (d) along a particular LOS. P/d is known as the rate of polarization. This relation is analogous to the rate of extinction, A_V/d , that is, the ratio of visual extinction (A_V) to distance (d), the mean of which is found to be $\approx 1.8 \text{ mag kpc}^{-1}$ (see, Whittet 2018). Recently, several researchers (e.g., Eswaraiah et al. 2011; Kumar et al. 2014;

Wang et al. 2017; Lee et al. 2018; Eswaraiah et al. 2019; Kumar et al. 2019) have studied the variation of P/d using the polarization data from Heiles (2000) and distances from Hipparchus catalogue (Van Leeuwen 2007) to show that P increases as a function of distance towards several targets in the solar neighbourhood. A common limitation of all such studies have been that they are confined to the solar neighbourhood or to particular distances where the clusters are located. In this context, studying P/d as a function of distance towards NGC 1893, being at a long distance beyond the solar neighbourhood, can shed light on the distribution of polarizing dust grains and presence of dust clouds along the LOS. It can also help to distinguish the foreground dust from that in the intra-cluster medium by revealing the distance at which the P/d shows a change.

Eswaraiah et al. (2011) have observed a constant magnetic field orientation beyond 1 kpc along the direction of NGC 1893. It was uncertain whether this is due to the uniform and dominant magnetic field in the foreground dust medium, or a truly constant field all up to the distance of NGC 1893. The revised distances determined from the recent *Gaia* EDR3 observations for both foreground and background fields and cluster members plus the polarization data provides an opportunity to study the variation of polarization and magnetic fields as a function of distance for a statistically significant sample of stars. It is possible to correct for the foreground contribution in the stokes vector form and therefore to study the variation in the dust properties and magnetic fields within a distant cluster. In this work, in addition to A_V versus P/A_V , we also examine d versus P/d utilizing the newly acquired polarization data along with the existing data (Eswaraiah et al. 2011), stellar distances from *Gaia* EDR3 (Bailer-Jones et al. 2021), and the extinction values from Bayestar19 three-dimensional (3D) dust map (Green et al. 2019).

Section 2 describes our new observations, and data reduction, in addition to archival data. Section 3 presents the analyses. Results are given in Section 4, including the fit with the broken power-law and Bayesian analyses on $A_V - P/A_V$ and $d - P/d$ plots, foreground subtraction, magnetic field morphology in NGC 1893, and the variation of various parameters of the confirmed cluster members as a function of radial distance, etc. We discuss our results in Section 5. Finally, Section 6 summarizes our findings and gives the conclusions.

2 OBSERVATIONS AND DATA REDUCTION AND ARCHIVAL DATA

2.1 Polarization data from ARIES IMAGING POLarimeter (AIMPOL)

Deeper I -band polarimetry observations of three fields towards NGC 1893 were carried out using the ARIES Imaging Polarimeter (AIMPOL) (Rautela et al. 2004) on 04 November 2013, mounted on the Cassegrain focus of the 104 cm Sampurnanand Telescope at ARIES in Nainital, India. In addition, we also reanalysed the six fields of I -band data towards NGC 1893 acquired on the two nights of 08 and 09 November 2008. The detailed reduction and analysis procedures of AIMPOL data can be found in Eswaraiah et al. (2011, 2012, 2013). Figure 1 depicts the field around NGC 1893. The six fields observed in 2008 and three fields in 2013 are indicated. Instrumental polarization of AIMPOL has been consistently estimated to be less than 0.1% (cf. Eswaraiah et al. 2011, 2012). The offset in the polarization angle is determined by observing the polarized standard star HD 25443 on 04 November 2013 for which the polarization and polarization angle in I -band are estimated $4.16 \pm 0.10\%$ and $134^\circ \pm 1^\circ$, respectively, consistent with the standard polarization $4.25 \pm 0.04\%$ and polarization

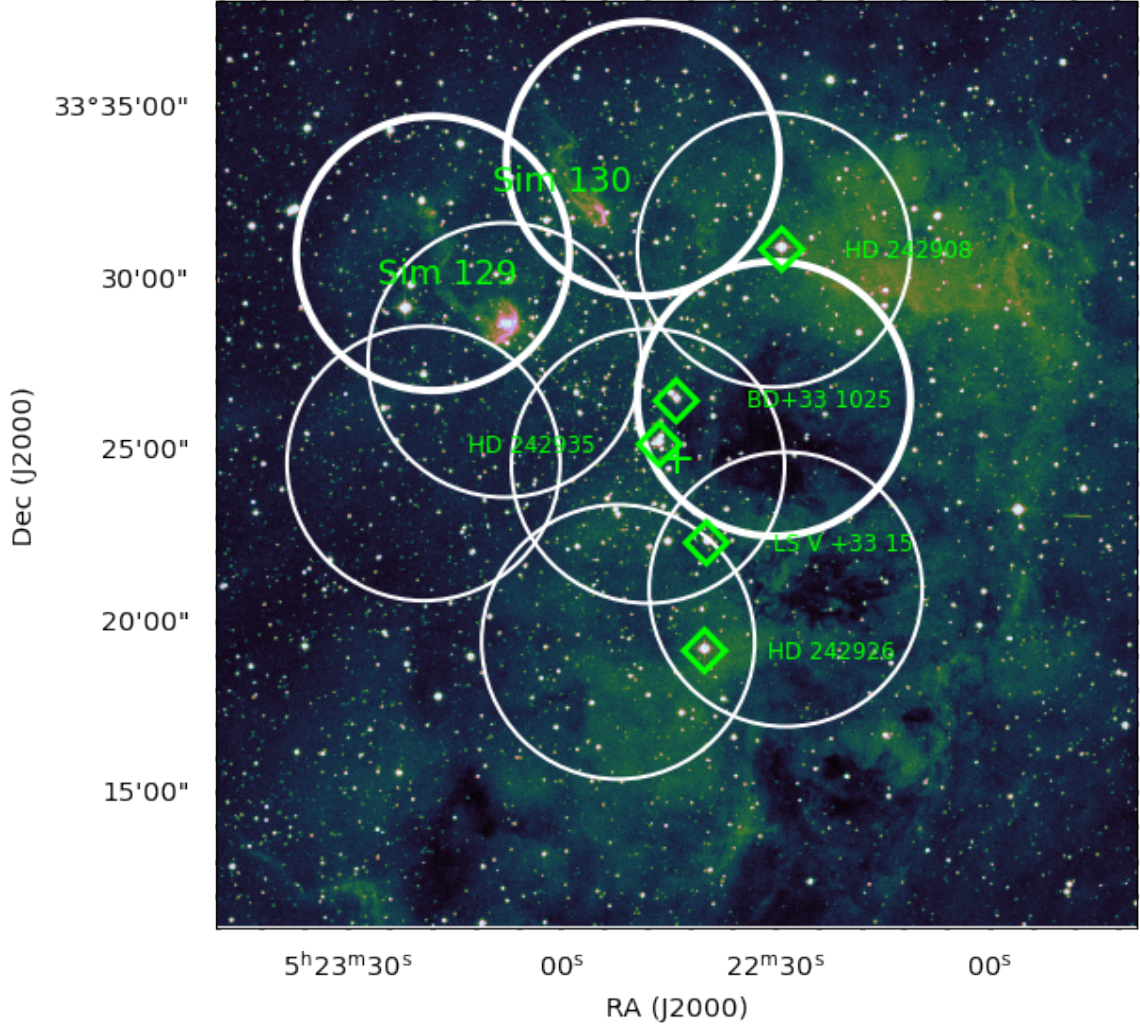


Figure 1. Colour composite image made using WISE $12\ \mu\text{m}$ (red), 2MASS K-band (green), and DSS R-band (blue) images of the star-forming region NGC 1893. Circles each with an $8'$ diameter, denote the observations acquired with AIMPOL in 2008 (six thin circles) and 2013 (three thick circles). Cluster centre $(RA, Dec)_{J2000}=(05^{\text{h}}:22^{\text{m}}:44^{\text{s}}, +33^{\circ}:24':42'')$ is marked with a green cross. Five O-type stars HD 242935, HD 242926, HD 242908, BD+33° 1025 and LS V +33° 15 are shown with green diamond symbols. The location of two emission nebulae Sim 129 and Sim 130 are also shown.

angle $134.2^{\circ} \pm 0.3^{\circ}$ in I -band for HD 25443 (Schmidt et al. 1992). All the polarization measurements, acquired on 04 November 2013, are corrected for the instrumental polarization and offset in the polarization angle. We found 40 common stars observed in both years of 2008 and 2013. The values of polarization (*Top*) and polarization angles (*Bottom*) measured in 2008 and 2013 are found to match closely with each other, as shown in Fig. 2. The stars shown with encircled filled circles are the two $H\alpha$ sources (Maheswar et al. 2007) and two Class II/Class III sources (Pandey et al. 2014). The measurements made in 2013 have smaller uncertainties owing to longer exposure time than those measured in 2008. Therefore, we adopt the measurements of 2013 for common sources in both epochs, and for the sources otherwise detected in only one epoch, we use the corresponding epoch data in our analysis.

Before we perform the analyses, we exclude the stars with possible intrinsic polarization based on the near-infrared (NIR) colour-colour diagram. Here, we assume that the intrinsic polarization can only be caused by the stars with circumstellar disks. Figure 3 shows the $[J-H]$ vs $[H-K_s]$ NIR colour-colour diagrams for 173 stars in I -band whose signal-to-noise ratio in polarization, P/σ_P , is greater than 3,

i.e., possibly with intrinsic polarization. The JHK_s photometric data have been obtained from 2MASS Point Source Catalogue (Cutri et al. 2003). Red and blue-filled circles are the Class II and Class III sources (Pandey et al. 2014). Small green-filled circles are the $H\alpha$ sources (Maheswar et al. 2007). Other NIR-excess sources are represented with encircled filled circles. In total, 21 stars, as mentioned above, may have intrinsic polarization. Therefore, out of 173 stars, we utilize the polarization data of 152 stars for the analyses. Figure 3 shows that most stars are not highly extinguished, but rather are distributed around the main sequence (MS) locus, with a few along the giant locus.

2.2 Distances from GAIA Early Data Release 3

We obtain the distances from Bailer-Jones et al. (2021). They have estimated distances using stellar parallaxes of 1.47 billion stars and have published *Gaia* Early Data Release 3 (hereafter *Gaia* ERD3). Even though *Gaia* ERD3 have a significant improvement in both precision and accuracy of astrometry and broad-band photometry, the majority of these stars are distant or faint that their parallax uncertainties are large, thereby precluding a simple inversion of stellar

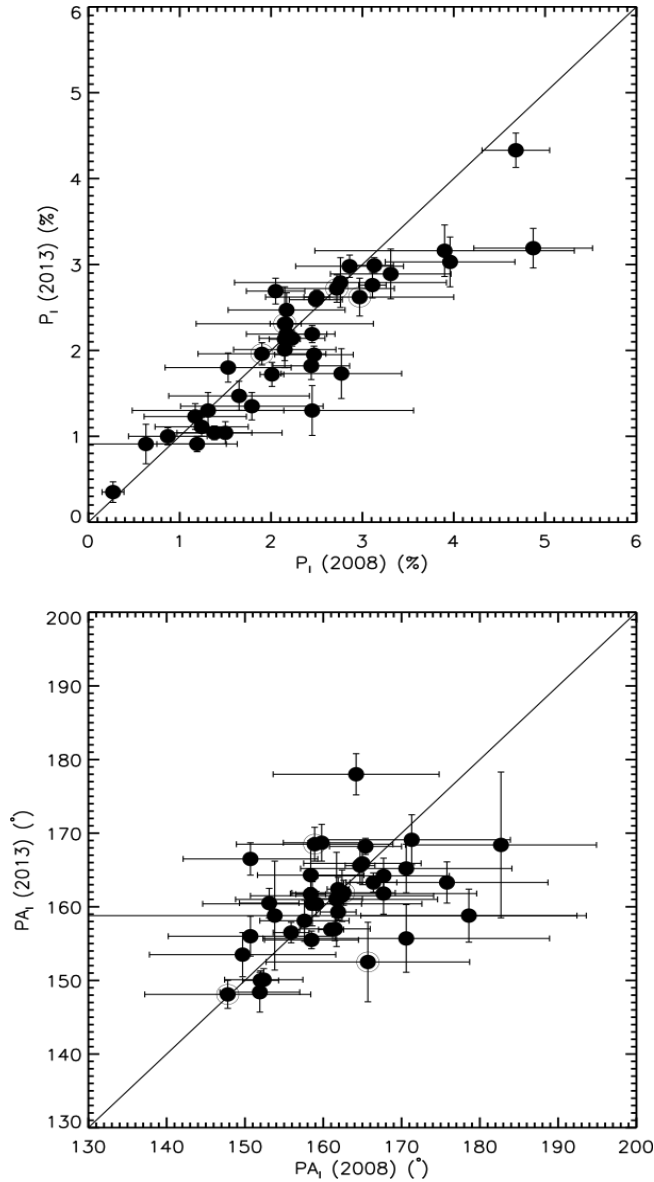


Figure 2. *Top:* $P_{I_{2008}}$ versus $P_{I_{2013}}$ of 40 common stars (filled circles). *Bottom:* $PA_{I_{2008}}$ versus $PA_{I_{2013}}$ (filled circles). The stars shown with encircled filled circles are the two $H\alpha$ sources and two Class II/Class III sources. The measurements of 2008 have relatively larger error bars than that of 2013. A thick straight line is drawn with a slope 1 ($= 45^\circ$) in both panels to check the one-to-one correlation between the polarization measurements at two epochs.

parallax to provide a distance. Therefore, they use a probabilistic approach to estimate the stellar distances using a prior constructed from a three-dimensional model of our galaxy, which includes the interstellar extinction and Gaia’s variable magnitude limit. Using this method, Bailer-Jones estimate two types of distances: (i) Geometric and (ii) Photogeometric. The first one uses the parallax together with a direction-dependent prior on distance, whereas the second one additionally uses the colour and apparent magnitude of a star, by exploiting the fact that stars of a given colour have a restricted range of probable absolute magnitudes and extinction. There exist geometric distances for 1.47 billion stars, and 92% of these stars have photogeometric distances. Tests on simulated data and external validation show that the photogeometric estimates generally have higher accu-

racy and precision for fainter and distant stars (Bailer-Jones et al. 2021). Therefore, we utilize photogeometric distances for our study. We cross-match the coordinates of 152 stars having polarization data with the Bailer-Jones catalogue towards NGC 1893. Within a $0.5''$ matching radius, we find 151 stars have photogeometric distances. They are given in Table 1.

2.3 Extinction data

We use the total extinction at V-band, A_V , data for our analyses. A_V data are extracted from Green et al. (2019). They use stellar photometry from optical Pan-STARRS 1 and near-infrared 2MASS photometry along with the *Gaia* DR2 parallaxes to infer distances and reddening to ~ 800 million stars. The reddening values of these stars are traced along different lines of sight, based on which they build a map of dust reddening in three-dimensions (Green et al. 2019) referred to as Bayestar19. Extinction towards a particular line of sight but at different distances can be extracted using the PYTHON based module, dust maps¹. The extinction map is structured as a set of sight lines, each of which contains multiple samples of cumulative dust reddening as a function of distance. Each sight line is identified by a HEALPix nsidc parameter and a nested pixel index. Within each sight line, cumulative reddening is given at discrete distances, spaced evenly in the distance modulus. Thus, for each pixel, it provides multiple samples from the posterior of dust reddening. It also gives quality assurance information for each pixel, i.e., whether the fit converges in the pixel and the minimum/maximum reliable distance moduli in the pixel (Green et al. 2019)².

We use the above-mentioned PYTHON package ‘dust maps’ which provides functions for querying and downloading the Bayestar19 3D dust map. The reddening values from the Bayestar19 dust map are obtained by providing the equatorial coordinates of stars and their distances as input. Thus, the reddening values corresponding to the maximum posterior density at a particular coordinate and distance are returned as output. Finally, the obtained reddening values are checked for their quality by examining whether the line-of-sight fit has converged in a given pixel and also whether the input distance is reliable within the range of the considered distances. Hence, we find the reddening values for 151 stars. Of which, 8 do not have reliable distance information, although their line-of-sight fits are converged. These eight stars are excluded from further analyses. Thus, the obtained reddening values for 143 stars are converted into extinctions using the following relations (Green et al. 2019)³:

$$\begin{aligned} E(g-r) &= 0.901 \cdot E_{\text{bayestar19}} \\ E(B-V) &= 0.981 \cdot E(g-r) \\ A_V &= R_V \cdot E(B-V) \end{aligned} \quad (1)$$

where $E_{\text{bayestar19}}$ is the reddening value obtained from Bayestar19 3D dust map. The $E(g-r)$ and $E(B-V)$ are the reddening values corresponding to $g-r$ and $B-V$ colours, A_V is the total extinction in the visual band, and R_V is the total-to-selective extinction of 3.1 (Savage & Mathis 1979; Cardelli et al. 1989). Since the dustmaps module does not provide uncertainties in reddening values, they are

¹ <https://dustmaps.readthedocs.io/en/latest/modules.html#module-dustmaps.bayestar>

² <https://dataverse.harvard.edu/dataset.xhtml?persistentId=doi:10.7910/DVN/2EJ9TX>

³ <http://argonaut.skymaps.info/usage#units>

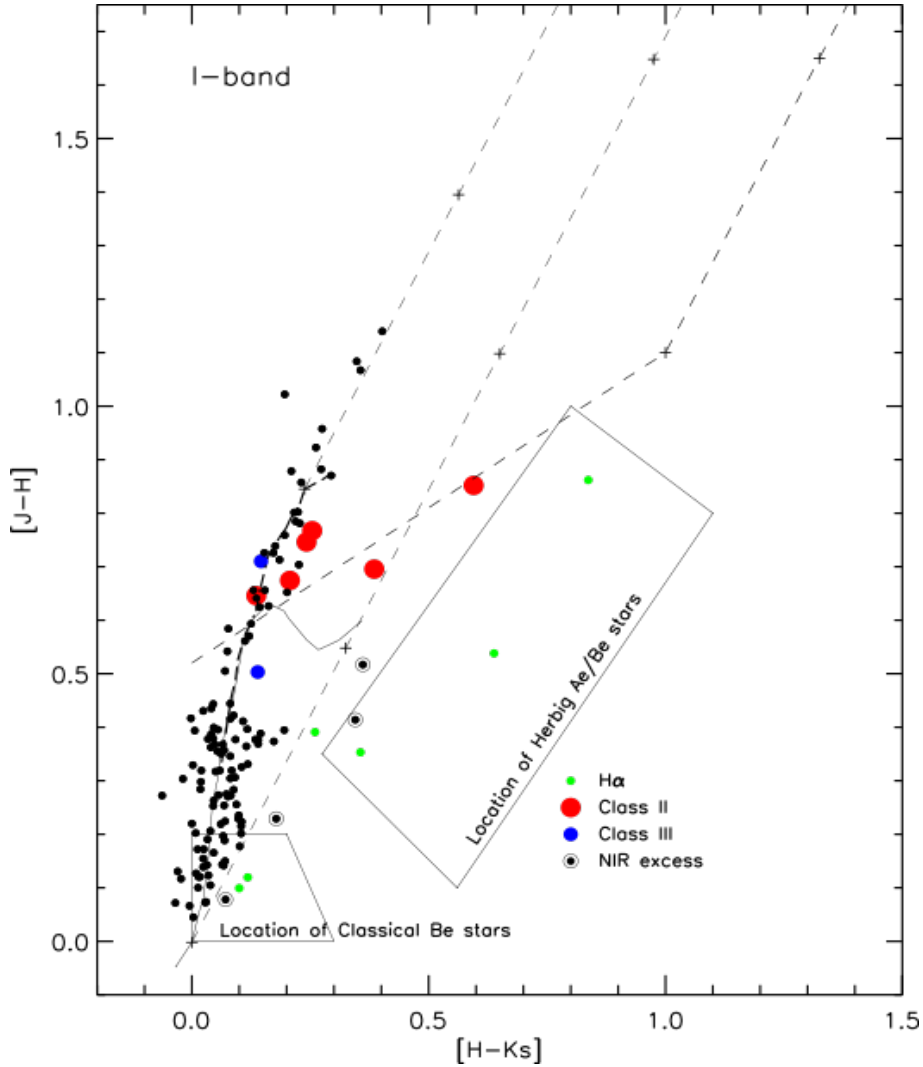


Figure 3. $[J-H]$ vs $[H-K_s]$ colour-colour diagram for 173 stars with I-band polarimetry. Red and blue-filled circles are Class II and Class III sources (Pandey et al. 2014). Small green-filled circles are the $H\alpha$ sources (Maheswar et al. 2007). Other NIR-excess sources were represented with encircled filled circles. The rest of the stars were shown with filled black circles. The solid and thick dashed curves represent the unreddened MS and giant branch (Bessell & Brett 1988), respectively. The dashed line indicates the locus of unreddened CTTSs (Meyer et al. 1997). The parallel dashed lines are the reddening vectors drawn from the tip (spectral type M4) of the giant branch (“upper reddening line”), from the base (spectral type A0) of the MS branch (“middle reddening line”) and from the tip of the intrinsic CTTS line (“lower reddening line”). The location of Be stars (cf. Dougherty et al. 1994) and the location of Herbig Ae/Be stars (cf. Hernández et al. 2005) are also shown.

extracted from Galactic Interstellar Extinction (GALExtin⁴; Amôres et al. 2021).

The maximum distance up to which the Bayestar19 3-D extinction map reddening values are reliable are estimated based on the distance at which the main sequence stars disappear along a particular LOS (Green et al. 2019). Since the stellar cluster NGC 1893 which is the subject of our study has a galactic latitude of -1.6342° , and is located close to the galactic midplane, the stellar number density in this region is significantly high (see, Figure 6 (a) of Sharma et al. 2007). So, there won’t be any dearth of main sequence stars at a particular distance along any LOS in this region. So the extinction (A_V) values we have extracted are valid up to a maximum of distance of 7 kpc which is the maximum photogeometric distance that we have used in our study.

To check the reliability of our reddening values obtained from Bayestar19 dust map (Green et al. 2019), we compare our reddening values with those from Bayestar15 (Green et al. 2015), Bayestar17 (Green et al. 2018) and Chen2019 (Chen et al. 2019) dust maps. Bayestar15 is a 3D map of dust reddening using Pan-STARRS 1 and 2MASS photometry based on a probabilistic approach, covering over a three-quarters of the sky. Bayestar17 is an improved version of Bayestar15 with the inclusion of additional Pan-STARRS 1 data, updated methodology and finer angular resolutions at high extinction regions. Chen2019 is another all sky map of dust reddening in 3D computed using the parallax and optical photometry from *Gaia* DR2 and infrared photometry from 2MASS and WISE. We find that most of our reddening values have a one to one correspondence with the reddening values obtained from these three dust maps, thereby attesting that our reddening values are reliable, and these A_V data are also given in Table 1.

⁴ www.galexin.org

2.4 Dust temperature using IRAS data

One of the key predictions of RAT theory is the positive correlation between the degree of polarization and dust temperature (Lazarian & Hoang 2007; Andersson et al. 2015). In order to examine whether this relation exists in NGC 1893 region, we extract the dust temperature map. Since the current target does not have *Herschel* data, we use Infrared Astronomical Satellite (IRAS) maps at 60 and 100 μm taken from SkyView Virtual observatory⁵. The dust temperature in each pixel of the IRAS image is obtained by assuming that the dust in a single beam is isothermal and that the observed ratio of 60 to 100 μm emission follows a blackbody radiation from dust grains at temperature T_d , modified by a power-law emissivity spectral index β . We use the following relation to derive T_d (Schnee et al. 2005):

$$R = 0.6^{-(3+\beta)} \cdot \frac{e^{144/T_d} - 1}{e^{240/T_d} - 1} \quad (2)$$

where R is the ratio of 60 to 100 μm flux densities, β is the dust emissivity spectral index which is approximately taken as 2, and T_d is the dust temperature at each pixel of the IRAS image. We cross-match the list of cluster stars having polarization measurements with the pixels of T_d map. Since the resolution of IRAS 60/100 μm , and hence the T_d map, is $2'$, we estimate mean and standard deviation in T_d over the pixels within $2'$ diameter around each star having polarization data.

3 ANALYSES

In this section we analyse how the polarization efficiency (P/A_V) varies as a function of extinction (A_V) and (ii) rate of polarization (P/d) varies as a function of distance (d). We used these analyses to examine whether the observed polarization measurements reveal the dust properties and magnetic field orientation of the foreground medium alone but not of the intra cluster medium, or of the dust grains distributed along the entire line of sight towards NGC 1893. After confirming the latter one that our polarization measurements consist of a contribution from the magnetically aligned dust grains in the intra-cluster medium, we try to quantify the foreground polarization contribution and subtract it from the measurements of cluster members. Eventually, we examine if there are changes in intrinsic polarization parameters, dust temperature, extinction, and polarization efficiency within the cluster region.

We model the plots with two different methods: – (i) broken power-law with a Levenberg-Marquardt non-linear least squares fitting method and (ii) broken power-law but with a Bayesian approach.

3.1 Broken Power-law fit

The relation $A_V - P/A_V$ is fitted with broken power-law of the form using *scipy-curve fit* module in PYTHON:

$$y = \begin{cases} a \left(\frac{x}{A_V^b} \right)^{b_1}, & \text{for } x \leq A_V^b \\ a \left(\frac{x}{A_V^b} \right)^{b_2}, & \text{for } x > A_V^b, \end{cases} \quad (3)$$

where x is A_V , A_V^b is the A_V at which the power-law breaks, and a is a coefficient. The b_1 and b_2 are power-law indices before and after

A_V^b . Similarly, the data of $d - P/d$ are also fitted with the broken power-law of the similar form to equation 3, where A_V and A_V^b are replaced with distance (d) and distance break d^b at which the power-law breaks, respectively. Figure 4 show the data and corresponding best fits for $A_V - P/A_V$ and $d - P/d$, respectively. The best-fit parameters are given in Table 2.

To check whether the broken power-law model of $A_V - P/A_V$ and $d - P/d$ fit the data better than a single power-law, we perform χ^2 -difference test and also estimate Akaike Information Criterion (AIC) and Bayesian Information Criterion (BIC) values. For $A_V - P/A_V$ with the difference in the degrees of freedom 2, the χ^2 -difference is 9.255 which is statistically significant as the corresponding p-value turns out to be 0.01 which is less than the statistically accepted 0.05 significance level, meaning that the model with more free-parameters or the broken power-law fits the data better. Furthermore, the AIC and BIC values for the broken power-law are lower than that of single power-law fit, confirming that the broken power-law is a better model than single power-law for $A_V - P/A_V$. For $d - P/d$ again with the difference in the degrees of freedom 2, the χ^2 -difference is 1.032, which is statistically insignificant as the corresponding p-value turns out to be 0.6 which is greater than the significance level of 0.05, implying that both models fit the data equally well. But lower values of AIC and BIC when compared to that of single power-law suggests that the broken power-law fits the data better. Therefore, broken power-law model can be accepted for fitting both $A_V - P/A_V$ and $d - P/d$ relations.

3.2 Bayesian Analyses

We have employed Bayesian analyses to confirm the results obtained from the broken power-law for $A_V - P/A_V$ and $d - P/d$ (above section). Bayesian analyses can help constrain the posterior distribution of all parameters based on the prior distributions and observational data expressed in the form of a likelihood function. We modeled the trends followed by $A_V - P/A_V$ and $d - P/d$ by combining broken power-law with Bayesian approach. The resulting analyses yield us the posterior mean fit along with the 95%, 68%, and 50% confidence regions (CRs), and the posterior probability density function (PDF) of each parameter as output as described in appendix A. The 95%, 68%, and 50% confidence regions (CRs) predicted by the posterior distribution for $A_V - P/A_V$ and $d - P/d$ plots are shown in Figure 5. From the figures, it is seen that the majority of the data fall well within 95% CR predicted by the posterior. The 94 % highest density interval (HDI) of each parameter are plotted to represent the data lying within 2σ uncertainties. The posterior PDF of the parameters derived from the Bayesian modelling is given in Figure 6. In Figure 6, α is a constant, β_1 , and β_2 are the power-law indices before and after the break in power-law for both the $A_V - P/A_V$. and $d - P/d$ plots. A_V^b and d^b are the A_V and d values at which the break occurs in $A_V - P/A_V$ and $d - P/d$ respectively. Similarly, σ is the dispersion in the data of P/A_V or P/d . More details about various parameters are given in the appendix A. The parameters constrained through the Bayesian analyses are reasonably more accurate than those obtained from the broken power-law alone. The constrained results from Bayesian analyses are listed in Table 3.

3.3 Differential plots in P and PA as a function of distance

Stokes parameters (Q and U) of all 151 stars are converted from P and PA (see, section 2.1) using the relations:

⁵ <https://skyview.gsfc.nasa.gov/current/cgi/titlepage.pl>

Table 1. Sample data table containing the year of observation, equatorial coordinates, distance, polarization data in I-band, 2MASS photometric data, optical extinction and temperature of the stars that we have used in this study.

SNo	Year	RA (J2000) (degree)	Dec (J2000) (degree)	Distance $\pm \sigma$ (kpc)	P $\pm \sigma$ (%)	PA $\pm \sigma$ (degree)
1	2008	80.665346	33.371732	3.00 \pm 0.16	2.12 \pm 0.18	151.0 \pm 2.0
2	2008	80.723805	33.392084	2.22 \pm 0.10	2.15 \pm 0.48	167.0 \pm 6.0
3	2008	80.719046	33.386870	2.32 \pm 0.12	2.37 \pm 0.49	164.0 \pm 6.0
4	2008	80.717592	33.384285	2.35 \pm 0.15	2.54 \pm 0.31	162.0 \pm 4.0
5	2008	80.688602	33.371345	0.86 \pm 0.01	1.46 \pm 0.23	174.0 \pm 4.0
6	2008	80.699181	33.368585	0.94 \pm 0.02	1.65 \pm 0.38	175.0 \pm 7.0
7	2008	80.741272	33.368718	2.68 \pm 0.78	2.79 \pm 0.49	158.0 \pm 5.0
8	2008	80.771703	33.359300	2.87 \pm 0.16	2.23 \pm 0.63	156.0 \pm 8.0
9	2008	80.622089	33.514012	3.01 \pm 0.21	2.86 \pm 0.12	147.0 \pm 1.0
10	2008	80.699321	33.476143	0.84 \pm 0.01	1.88 \pm 0.21	165.0 \pm 3.0
11	2008	80.751907	33.496616	2.51 \pm 0.12	2.79 \pm 0.27	161.0 \pm 3.0
12	2008	80.731302	33.487467	3.10 \pm 0.25	3.39 \pm 0.58	159.0 \pm 5.0
13	2008	80.767385	33.470600	2.92 \pm 0.17	3.12 \pm 0.48	155.0 \pm 4.0
14	2008	80.725975	33.445086	2.81 \pm 0.16	3.00 \pm 0.59	154.0 \pm 6.0
15	2008	80.782324	33.467270	2.14 \pm 0.12	2.82 \pm 0.54	159.0 \pm 6.0
16	2008	80.762063	33.454518	1.63 \pm 0.08	2.25 \pm 0.69	159.0 \pm 9.0
17	2008	80.741849	33.443460	1.47 \pm 0.50	2.36 \pm 0.26	160.0 \pm 3.0
18	2008	80.713246	33.426608	3.29 \pm 0.28	3.03 \pm 0.73	150.0 \pm 7.0
19	2008	80.744290	33.400895	2.73 \pm 0.22	3.47 \pm 0.52	160.0 \pm 4.0
20	2008	80.765901	33.400821	3.28 \pm 0.20	2.90 \pm 0.46	161.0 \pm 5.0

SNo	J $\pm \sigma$ (mag)	H $\pm \sigma$ (mag)	K $\pm \sigma$ (mag)	A _V $\pm \sigma$ (mag)	Temperature $\pm \sigma$ (K)
1	9.00 \pm 0.02	8.89 \pm 0.02	8.79 \pm 0.02	1.67 \pm 0.12	28.72 \pm 0.77
2	11.58 \pm 0.02	11.57 \pm 0.02	11.54 \pm 0.02	0.79 \pm 0.02	-
3	11.82 \pm 0.02	11.76 \pm 0.02	11.71 \pm 0.02	0.79 \pm 0.02	-
4	11.02 \pm 0.02	10.99 \pm 0.02	10.99 \pm 0.02	0.79 \pm 0.02	-
5	10.13 \pm 0.03	10.06 \pm 0.02	9.99 \pm 0.02	0.63 \pm 0.1	-
6	10.92 \pm 0.02	10.58 \pm 0.02	10.49 \pm 0.02	0.63 \pm 0.1	-
7	11.91 \pm 0.02	11.82 \pm 0.02	11.81 \pm 0.02	1.07 \pm 0.09	-
8	11.44 \pm 0.02	10.70 \pm 0.02	10.50 \pm 0.02	1.24 \pm 0.11	-
9	8.28 \pm 0.02	8.25 \pm 0.03	8.18 \pm 0.02	1.07 \pm 0.09	30.87 \pm 0.31
10	8.82 \pm 0.02	8.22 \pm 0.02	8.06 \pm 0.02	0.68 \pm 0.02	-
11	11.64	11.53	11.43 \pm 0.03	0.79 \pm 0.05	-
12	12.48 \pm 0.02	12.09 \pm 0.02	11.94 \pm 0.02	1.15 \pm 0.05	31.21 \pm 0.4
13	12.77	12.57 \pm 0.05	12.47 \pm 0.04	0.88 \pm 0.07	-
14	12.80 \pm 0.03	12.68 \pm 0.04	12.62 \pm 0.03	0.87 \pm 0.05	-
15	12.48 \pm 0.02	12.31 \pm 0.03	12.24 \pm 0.02	0.83 \pm 0.02	-
16	12.77 \pm 0.02	12.43 \pm 0.02	12.34 \pm 0.02	0.82 \pm 0.02	-
17	11.46 \pm 0.02	11.32 \pm 0.02	11.26 \pm 0.02	0.82 \pm 0.03	-
18	13.44 \pm 0.03	13.33 \pm 0.04	13.22 \pm 0.04	2.16 \pm 0.04	30.58 \pm 0.64
19	12.40 \pm 0.02	12.26 \pm 0.02	12.21 \pm 0.02	0.86 \pm 0.07	-
20	11.90 \pm 0.02	11.24 \pm 0.02	11.05 \pm 0.02	1.15 \pm 0.08	31.64 \pm 0.53

Table 2. Best fit parameters, based on the broken power-law, for $A_V - P/A_V$ and $d - P/d$

Relation	a	b_1	b_2	A_V^b or d^b
$P/A_V - A_V$	2.6 \pm 0.2	0.01 \pm 0.19	-1.0 \pm 0.1	0.96 \pm 0.09 mag
$P/d - d$	1.1 \pm 0.1	-0.8 \pm 0.1	-0.3 \pm 0.1	1.5 \pm 0.3 kpc

Table 3. Best fit parameters based on broken power-law Bayesian model for $A_V - P/A_V$ and $d - P/d$

Relation	α	β_1	3% HDI (β_1)	97% HDI (β_1)	β_2	3% HDI (β_2)	97% HDI (β_2)	A_V^b or d^b	3% HDI (A_V^b or d^b)	97% HDI (A_V^b or d^b)	σ
$P/A_V - A_V$	2.8	0.04	-0.26	0.18	-0.9	-1.2	-0.7	0.9 mag	0.8 mag	1 mag	0.6%/mag
$P/d - d$	1.3	-0.8	-0.9	-0.6	-0.6	-0.7	-0.4	1.5 kpc	0.8 kpc	2.3 kpc	0.3%/kpc

HDI: Highest density interval

$$Q = P \cos(2PA)$$

$$\text{and } U = P \sin(2PA). \quad (4)$$

To understand the change in polarization parameters in response to

the dust layers along the line of sight, we construct differential plots in Stokes parameters $\Delta Q (= Q_{i+1} - Q_i)$ and $\Delta U (= U_{i+1} - U_i)$ versus distance $_{i+1}$, where i is an immediate foreground star to $(i+1)^{th}$ star. These ΔQ and ΔU are converted into ΔP and ΔPA using the

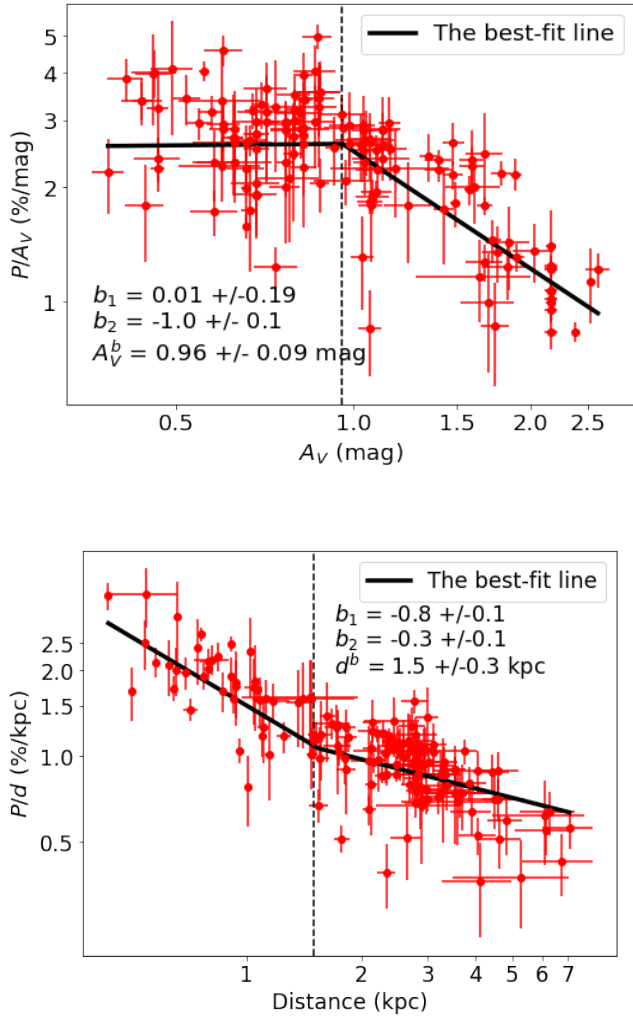


Figure 4. A_V versus P/A_V plot (Top) and d versus P/d plot (Bottom). Best fit broken power-law is denoted with thick line. The dotted vertical line corresponds to A_V^b and d^b at which the power-law breaks. Best-fit parameters are also overlaid.

relations:

$$\begin{aligned} \Delta P &= \sqrt{\Delta Q^2 + \Delta U^2} \\ \Delta PA &= 0.5 \cdot \arctan\left(\frac{\Delta U}{\Delta Q}\right) \cdot \left(\frac{180}{\pi}\right) \end{aligned} \quad (5)$$

The corresponding errors are given by:

$$\begin{aligned} \sigma_{\Delta P} &= \frac{1}{\Delta P} \cdot \sqrt{(\Delta Q \cdot \sigma_{\Delta Q})^2 + (\Delta U \cdot \sigma_{\Delta U})^2} \\ \sigma_{\Delta PA} &= \frac{1}{2\Delta P^2} \cdot \sqrt{(\Delta Q \cdot \sigma_{\Delta U})^2 + (\Delta U \cdot \sigma_{\Delta Q})^2} \cdot \left(\frac{180}{\pi}\right) \end{aligned} \quad (6)$$

These analyses help visualize the changes in P and PA across the dust layers lying between $(i+1)^{th}$ and i^{th} star (see [Eswaraiah et al. 2019](#), see their Figure 4 and Section 3.2 for more details on differential plots).

The differential density plots shown in the Figure 7 reveal a clear transition in both ΔP and ΔPA at a distance of ~ 2 kpc. To elucidate further, the information on probability density and frequency distribution are shown with gray/black background and histograms,

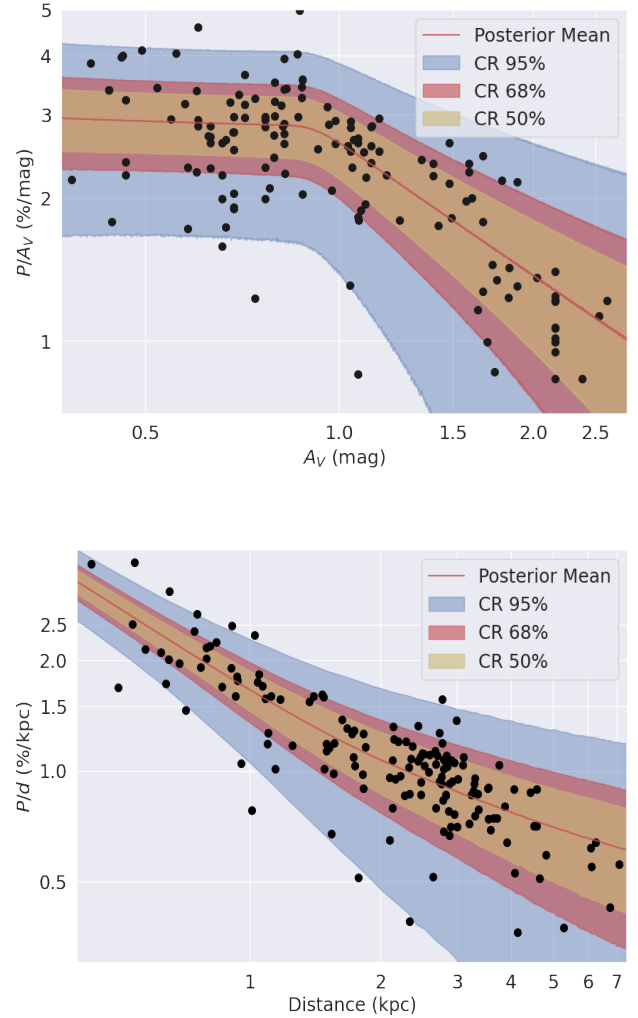


Figure 5. Comparison between the Bayesian posterior prediction and the observations for A_V versus P/A_V (Top) and d versus P/d (Bottom). The black line and coloured regions show the mean, 95%, 68%, and 50% confidence regions, predicted by the posteriors as shown in Top and Bottom panels of Figure 6 respectively.

respectively. Note that while constructing histograms we use bin sizes of 0.25%, 10°, and 350 pc for ΔP , ΔPA , and distance $_{i+1}$ respectively.

To confirm this transition occurring at a distance of ~ 2 kpc, we apply the Gaussian Mixture Model (GMM) analyses (e.g. [Krone-Martins et al. 2010](#); [Ducourant et al. 2017](#); [Melchior & Goulding 2018](#); [Cantat-Gaudin et al. 2019](#)) on the differential plots, by providing ΔP , ΔPA , and, distance $_{i+1}$ as input using the *scikit-learn* module in PYTHON. GMM is a probabilistic model which assumes that the data instances are generated from several Gaussian distributions each with an unknown set of parameters, i.e. mean and covariance values. Since GMM is a powerful grouping algorithm, we use it for grouping stars based on their properties. The GMM does this by assigning probability for each star being part of a separate group, say group-0 or group-1. For this purpose, GMM uses an Expectation-Maximization (EM) algorithm. The EM algorithm starts off by assigning the group parameters randomly to the given set of stars and is followed by two steps: expectation and maximization, which are repeated until it achieves convergence. In the expectation step, EM computes the probability for each star to belong to each group based on the current

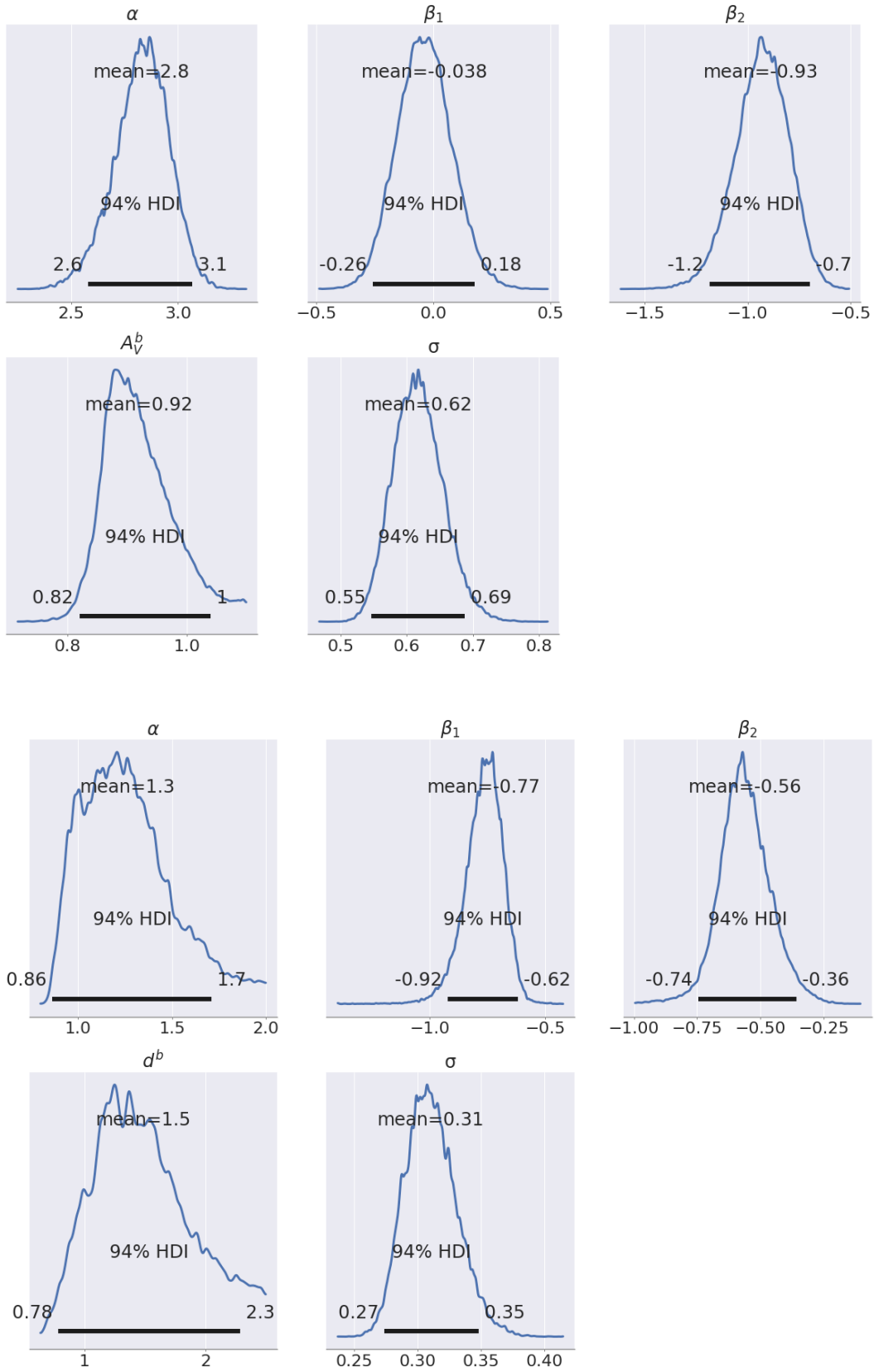


Figure 6. PDF of the model parameters derived using Bayesian model fitting of A_V versus P/A_V (Top) and d versus P/d (Bottom) respectively.

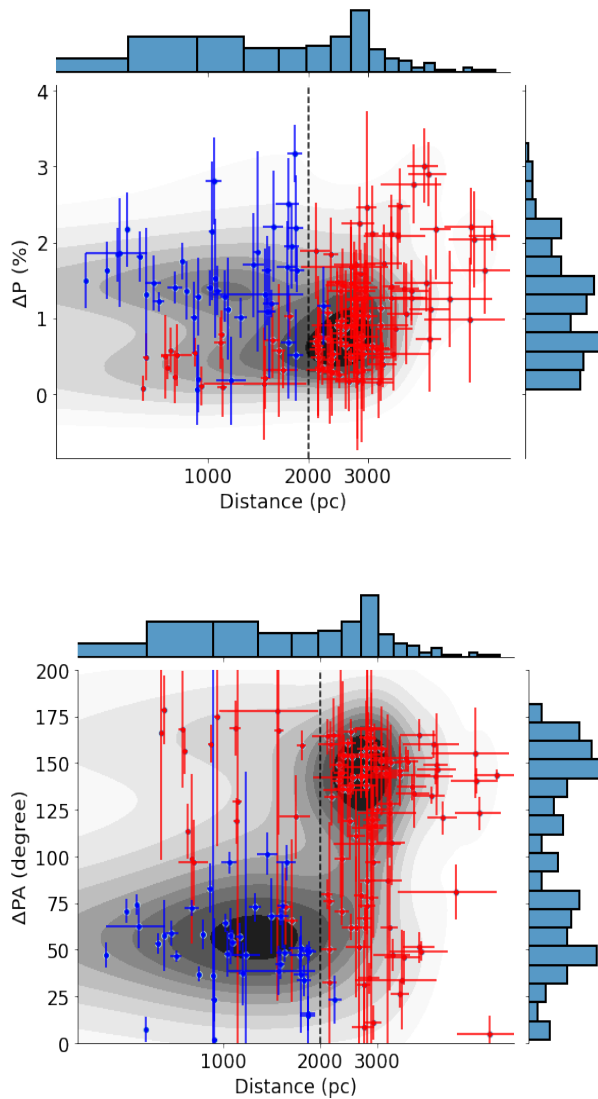


Figure 7. The differential density plots: distance versus ΔP (Top) and ΔPA (Bottom). The darker background is corresponding to the higher probability density, whereas the lighter density for lower probability density. Two groups of stars: group-0 (red) and group-1 (blue) identified by the GMM are overlaid. The vertical dotted line denotes 2 kpc where the transition is observed. Two-dimensional histograms in each panel are also shown.

group parameters. Then in the maximization step, it updates each group based on all the stars in the group, with each star weighted by the probability that it belongs to that group. The GMM resulting group of stars (0 and 1) are shown using red and blue symbols in Figure 7.

It is evident that two distributions exist in both plots of Figure 7 and are clearly separated at ~ 2 kpc. The darkest probability density centred around 3 kpc could be related to the cluster members of NGC 1893. Note that a marked shift from a lower to higher value of ΔPA at ~ 2 kpc can be seen in Figure 7 (Bottom). These findings are in accordance with the distance break obtained at 1.5 ± 0.5 kpc based on the broken-power law and broken power-law Bayesian models (cf. Sections 3.1 and 3.2).

3.4 Confirmation of two groups of stars

To confirm the presence of two groups of stars as proposed in Section 3.3, we again employ GMM analyses. For this we utilize proper motion (μ_{RA} and μ_{Dec}), Stokes parameters (Q and U), and stellar parallax data as input parameters. The proper motion data are obtained from the *Gaia* EDR3 catalogue, whereas the Stokes parameters using equation 4. The GMM resulting groups (0 and 1) are shown using red and blue symbols in Figures 8 and 9. The 1σ , 2σ and 3σ confidence ellipses of group-0 and group-1 stars are also shown in Figure 8.

Figure 8 (Top) shows the clear distributions predicted by GMM – cluster members and background stars as depicted in red exhibit a smaller amounts of proper motion as they fall close (0, 0), whereas the foreground stars, shown with blue, exhibit larger amounts of proper motion with a scattered distribution. This is also evident from the larger confidence ellipses for foreground stars when compared to cluster and background stars.

Similarly, the Stokes plane diagram (Q vs U) shown in Figure 8 (Bottom) also reveals two distributions. Cluster members shown in red are grouped together as their polarization properties are similar. This is because they are believed to be formed out of a same parental molecular cloud at the similar ages, and also their distances and amounts of extinction will also be similar. Owing to these, when the light from cluster members passes through the common layers of aligned dust grains and magnetic fields, their polarization properties will be similar and as a result they exhibit clustered distribution in the Stokes plane. In case of a negligible amount of polarizing dust in the background medium (that lies between cluster members and background stars), their position in the Stokes plane may merge with (or scatter from) those of cluster members given the magnetic field orientation is similar (or different) from that in the cluster. Foreground stars with blue fall close to (0, 0) and also show a scattered distribution in the Stokes plane depending upon the amount of extinction (hence polarization) present in the foreground medium and the morphology of magnetic field in the foreground medium (eg., Eswaraiah et al. 2011). Therefore, distance versus proper motions plots (Figure 9) demonstrate two groups being separated at 2 kpc, with a very few stars from one group falling into the another one.

4 RESULTS

4.1 A_V versus P/A_V

Based on the broken power-law fitting on $A_V - P/A_V$, shown in Figure 4 (Top), we find that the polarization efficiency (P/A_V) remains constant up to a threshold extinction, A_V^b , of 0.96 ± 0.09 mag with a power-law index of 0.01 ± 0.19 . For $A_V > 0.96$ mag the dust polarization efficiency decreases with a power-law index of -1.0 ± 0.1 . The Bayesian analysis also reveals similar results as those obtained from broken power-law fits (see Table 3) with A_V^b occurring at 0.9 mag with a 97 % highest density interval (HDI) of 1 mag as shown in Figure 5 (Top). From this, we infer the existence of two dust populations. One with $A_V < 0.9$ mag exhibits a higher polarization efficiency than the other with $A_V > 0.9$ mag.

4.2 d versus P/d

The broken power-law over the data of $d - P/d$, shown in Figure 4 (Top), reveals a steeply decreasing trend by the rate of polarization up to a break distance, d^b , of 1.5 ± 0.3 kpc by following an index of -0.8 ± 0.1 . Thereafter, the rate of polarization still decreases, but with a shallower power-law index of -0.3 ± 0.1 . The Bayesian

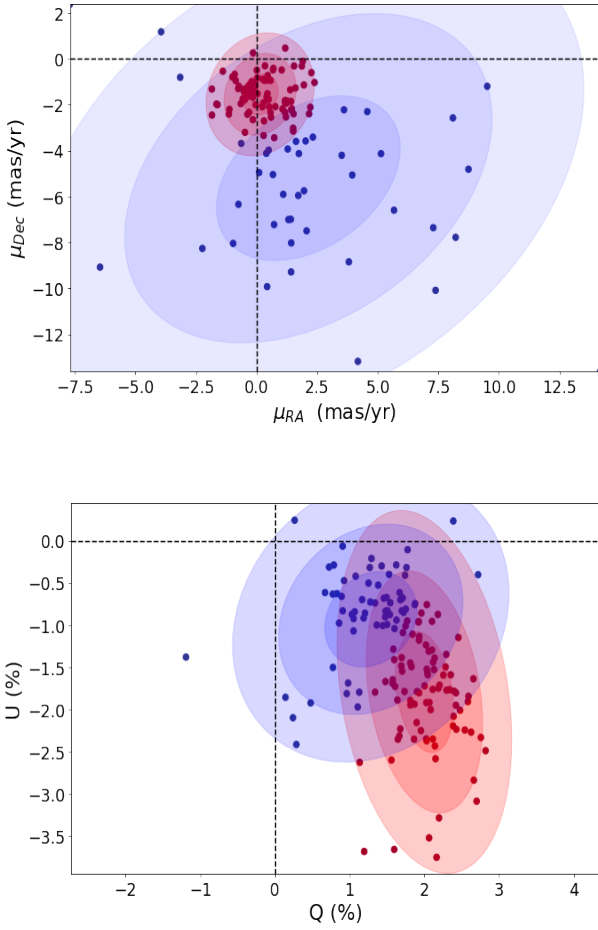


Figure 8. Proper motion (*Top*) and Stokes plane (*Bottom*) plots identified using GMM method. The group-0 members (red) are the cluster members and background stars, and group-1 members (blue) are the foreground stars. The 1σ , 2σ and 3σ confidence ellipses of group-0 and group-1 members are also shown.

analysis on this plot also exhibits similar results as those obtained from broken power-law fits as per the Table 3. Therefore, we confirm the presence of two dust populations, as proposed in Section 4.1, that they are separated at the distance of ~ 1.5 kpc. The first dust population span below 1.5 kpc exhibits weaker rate of polarization, whereas the second dust population with distance > 1.5 kpc exhibits a higher rate of polarization.

Hereafter, we consider 2 kpc as the boundary where the broken power-law and Bayesian analyses (Sections 3.1 and 3.2), differential plots (Section 3.3), and GMM analyses on Stokes parameters and proper motion data (Section 3.4), altogether hint a change in the polarization properties and dust extinction. Based on these, we categorize stars with $d < 2$ kpc and $A_V < 1$ mag as the foreground stars tracing the foreground dust, whereas the stars with $d > 2$ kpc and $A_V > 1$ mag as cluster members and background stars tracing Perseus arm dust (hereafter, Perseus dust) towards the line of sight of NGC 1893.

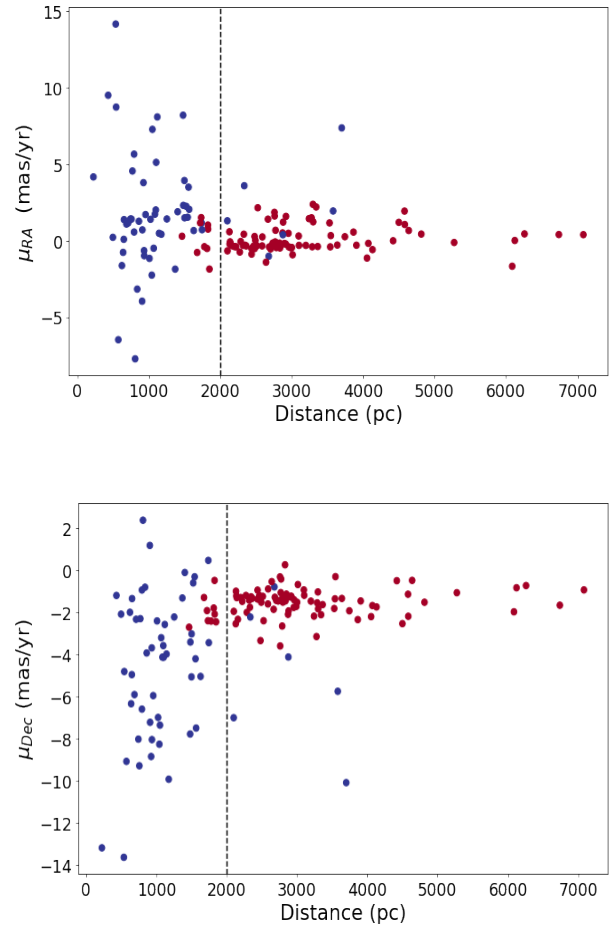


Figure 9. Distance versus μ_{RA} (*Top*) and μ_{Dec} (*Bottom*). In both figures (top and bottom panels), most of the group-0 members (red) are located after 2 kpc indicating that they are the cluster members and background stars, whereas most of the group-1 members (blue) are located up to 2 kpc which indicates that they are the foreground stars. The black vertical dotted line denotes distance of 2kpc.

4.3 Foreground contribution and intrinsic polarization measurements of the intra-cluster medium

Power-law indices of $A_V - P/A_V$ (Section 4.1) imply that although foreground dust is a major contributor to polarization, it is not a sole contributor, and that there is a non-negligible contribution from Perseus-dust. In contrast, the power-law indices of $d - P/d$ (Section 4.2) suggest a higher polarization rate for Perseus-dust than foreground dust. Therefore, current observations indeed can reveal the polarization properties of intra-cluster medium of NGC 1893 if we do the foreground correction. Based on this assumption of a small and non-negligible polarization contribution from the intra-cluster medium, we subtract the contribution of foreground polarization and extract the intrinsic polarization properties (P_{int} and PA_{int}).

To estimate the foreground polarization measurements, we perform weighted linear fits on the Stokes parameters versus distance plots by considering the data up to 2 kpc. From the fit we have estimated the resultant Stokes parameters at 2 kpc, which are treated as foreground Stokes parameters, Q_{fg} and U_{fg} . These are vectorially subtracted from the Stokes parameters of stars distributed beyond 2 kpc and obtain the intrinsic Stokes parameters using the following relations:

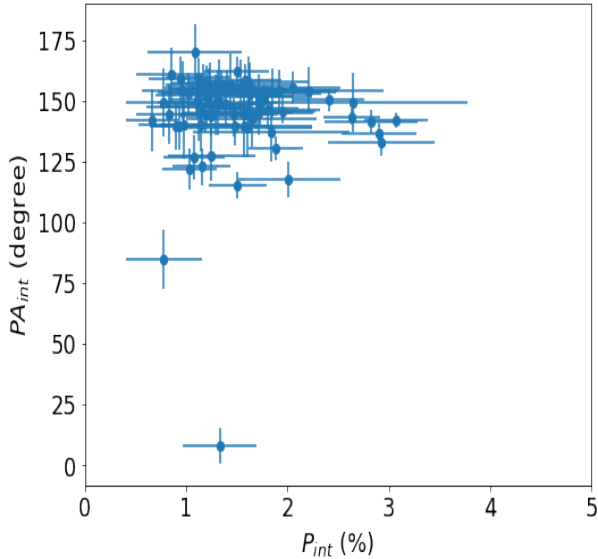


Figure 10. P_{int} versus PA_{int} scatter plot after applying signal-to-noise ratio condition with the criteria of $P_{int}/\sigma_{P_{int}} < 2$

$$\begin{aligned} Q_{int} &= Q - Q_{fg} \\ U_{int} &= U - U_{fg} \end{aligned} \quad (7)$$

The intrinsic polarization (P_{int}) and intrinsic polarization angle (PA_{int}) of the Perseus-dust and its corresponding errors are derived using equations 5 and 6. We have excluded 21 stars with lower signal-to-noise ratio with criteria of $P_{int}/\sigma_{P_{int}} < 2$. The resulting P_{int} and PA_{int} values are shown in Figure 10. To infer the variation in the intrinsic polarization properties of the intra-cluster medium, we further exclude 38 stars whose distances lie between 2 and 3 kpc. We assume that the remaining 32 stars lying beyond 3 kpc can trace the dust properties of the intra-cluster medium.

4.4 Effect of foreground polarization and magnetic field morphology in NGC 1893

To examine the effect of foreground polarization subtraction, we construct cumulative distribution function (CDF) and Probability distribution function (PDF) for the polarization measurements before (P and PA) and after (P_{int} and PA_{int}) foreground subtraction. These CDF and PDF plots for P and P_{int} and PA and PA_{int} are shown in Figure 11. To verify whether the mentioned pair of distributions (P versus P_{int} and PA versus PA_{int}) are similar or not, we perform Kolmogorov-Smirnov (KS) test on the PDFs and CDFs. KS test yield two parameters – statistic and p-value, of which p-value is the most important parameter as it infers whether a pair of distributions are drawn from a same parental distribution or not. A smaller p-value denotes that the two distributions are different, such that they are not drawn from a same parental distribution. KS-test on CDFs and PDFs of P vs. P_{int} and PA vs. PA_{int} suggest smaller p-values (6.8e-10 and 5.2e-05). These imply P and PA are entirely different from P_{int} and PA_{int} , respectively, and are not drawn from the same distributions.

The above findings are further corroborated by the observed different Gaussian means for polarization and polarization angles, as indicated in Figure 12. We observe two noticeable differences in the intrinsic polarization properties of the intra-cluster medium after the

foreground subtraction: (a) the Gaussian mean of P_{int} is systematically smaller than that of P , as clear from Figure 12 (Top) due to removal of the foreground contribution, and (b) Gaussian means of PA_{int} and PA are similar within the standard deviations albeit with a wider PA_{int} distribution indicating slight change in the magnetic field morphology in NGC 1893.

Figure 13 (Left) shows the polarization vector map delineating the magnetic field morphology before (red) and after (yellow) foreground subtraction. The length of the vector is proportional to the degree of polarization (P or P_{int}), whereas the orientation of the vector corresponds to the magnetic field orientation (PA or PA_{int}) with reference to equatorial north but increasing towards the east. Therefore, the effect of foreground subtraction on the polarization properties of intra-cluster medium can be seen as a systematic reduction in fraction of polarization but without a significant difference in the overall mean magnetic field orientation in NGC 1893. Moreover, magnetic field in the foreground (circular mean = $156^\circ \pm 6^\circ$) and intra cluster medium (circular mean = $147^\circ \pm 11^\circ$) are nearly similar within the uncertainties, indicating the presence of uniform magnetic field orientation towards the direction of NGC 1893. The overall mean field orientation in the intra-cluster medium is nearly parallel to the position angle of the Galactic plane, 141° , at $b = -1.53^\circ$ towards the direction of NGC 1893. The mean magnetic field orientation inferred by *Planck* dust continuum polarization data at $850 \mu\text{m}$ ⁶ is found to be $153^\circ \pm 9^\circ$ (Planck Collaboration et al. 2016a). The overall magnetic field morphology, based on *Planck*/353 GHz low-resolution ($5'$) dust polarization data, is found to be uniform as shown in the Figure 13 (Right). This overall geometry is consistent with the magnetic field morphology inferred from optical data.

4.5 Changes in the intrinsic polarization parameters and other relevant parameters in the cluster region

In order to examine the change in the polarization parameters in response to other crucial parameters in the star forming region, we have plotted radial distance (with respect to central coordinates of NGC 1893) versus PA_{int} , P_{int} , T_d , $A_{V_{int}}$, and $P_{int}/A_{V_{int}}$ as shown in Figure 14. Here, $A_{V_{int}}$ is the intrinsic total extinction of stars with distance greater than 3 kpc after correcting for a mean foreground extinction of 0.97 mag. T_d is the dust temperature and $P_{int}/A_{V_{int}}$ is the intrinsic polarization efficiency. To make the trends in the plot more clear, we over plot Figure 14 with curves drawn using the locally weighted scattered smoothing (LOWESS) algorithm (Cleveland 1979) from *statsmodels* package in PYTHON. We use a ‘frac’ parameter of 0.5 to draw the LOWESS curves over all the panels. The corresponding 1- σ regions (green) bounded by the $+\sigma$ (orange) and $-\sigma$ (green) lines are also shown in all the plots.

From Figure 14, the magnetic field orientation, based on the majority values of PA_{int} , is found to be rather uniform without a significant change in the intra cluster medium of NGC 1893 region. The P_{int} shows a constant trend up to $\sim 500''$, and afterwards it exhibits a scattered distribution. Dust temperature is tending to increase up to $\sim 500''$, and thereafter it decreases. $A_{V_{int}}$ shows a decreasing trend

⁶ The *Planck* polarization data comprising of Stokes I , Q , and U maps were extracted from *Planck* Public Data Release 2 (Planck Collaboration et al. 2016b) of Multiple Frequency Cutout Visualization (PR2 Full Mission Map with PCCS2 Catalog; <https://irsa.ipac.caltech.edu/applications/planck/>). The pixel size and beam size were $\sim 1'$ and $\sim 5'$, respectively. We have processed the data and obtained the magnetic field map using the procedures presented in Section 3.4 of Baug et al. (2020) and references therein.

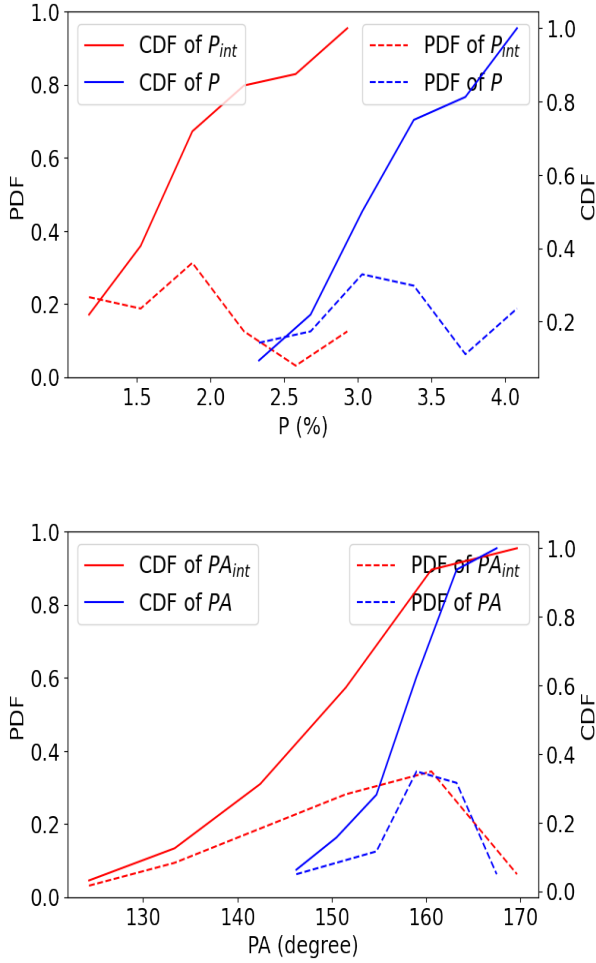


Figure 11. Probability Density Function (PDF) and Cumulative Distribution Function (CDF) of P , P_{int} (Top) and PA , PA_{int} (Bottom) respectively.

up to $\sim 400''$, and thereafter it remains nearly constant. The intrinsic polarization efficiency, $P_{int}/A_{V_{int}}$, exhibits an increasing trend up to $\sim 400''$, and thereafter it shows a scattered distribution. Except for PA_{int} and P_{int} , all parameters show a clear change within the region spread over $\sim 400'' - 500''$ in NGC 1893. This is where the two nebulae Sim 129 and Sim 130 are forming due to radiative driven implosion by the UV radiation emanating from the O/B- type stars (Maheswar et al. 2007; Sharma et al. 2007). Changes in various parameters are found to be happening in the area lying between two concentric circles of radii $400''$ and $500''$ as shown in Figure 13 (Left). We note here that both tips of Sim 129 and 130, and the shell-like structure surrounding the cluster centre, seem to be formed as a consequence of swept material out of expanding ionization and shock fronts from the O/B type stars formed near the cluster centre.

5 DISCUSSION

From the broken power-law fit and Bayesian analyses of $A_V - P/A_V$ (see Figures 4 and 5 and Section 4.1) we show that polarization efficiency (P/A_V) exhibits a constant trend as a function of extinction (A_V) up to threshold extinction value $A_V^b \sim 0.9$ mag with a power-law index of ~ 0 (see, Table 3). This constant trend implies all the dust grains are aligned uniformly, and they polarize the stellar light up

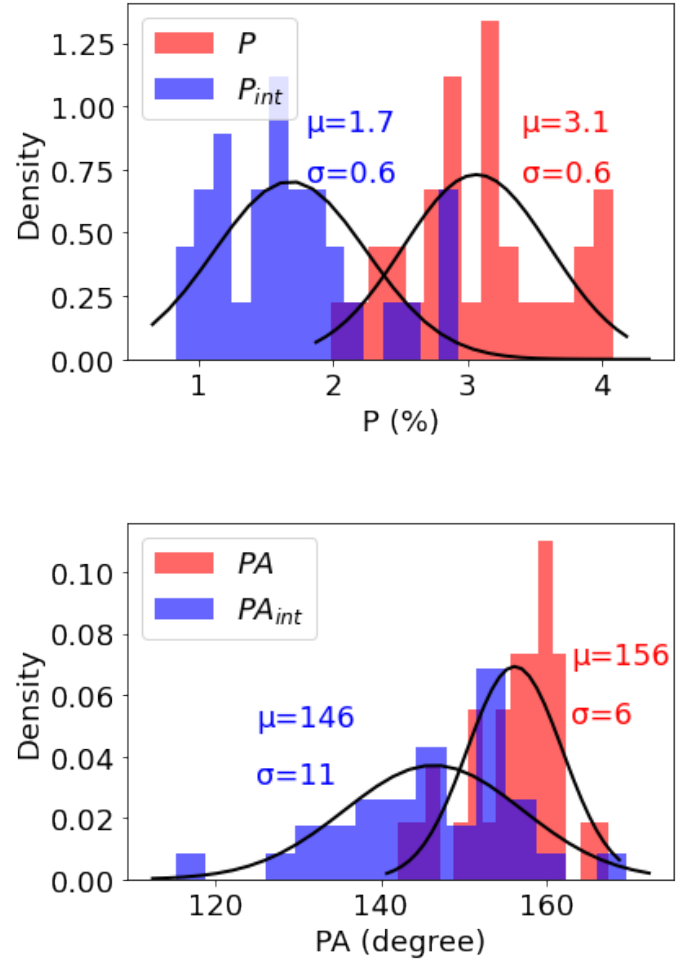


Figure 12. Histogram with Gaussian fits (shown in figure as a thick black line) of P , P_{int} (Top) and PA , PA_{int} (Bottom). The mean values and the standard deviations corresponding to P , P_{int} and PA , PA_{int} are shown in red and blue colour fonts respectively.

to the same degree at all the dust layers located up to $A_V \sim 0.9$ mag. For $A_V > 0.9$ mag, polarization efficiency declines steeply with 94% highest density interval of indexes ranging from -1.2 to -0.7 (see Figure 6 (Top)), indicating poorly aligned dust grains. A number of studies have probed the variation of P/A_V as a function of A_V towards several dark clouds like Taurus and Rho Ophiuchus molecular cloud complexes using near-infrared observations. Majority of these studies find a drop in P/A_V as a function of A_V with a typical power law index close to -0.5 (eg., Tamura et al. 1987; Gerakines et al. 1995; Whittet et al. 2008; Chapman et al. 2011; Cashman & Clemens 2014). Some studies (eg., Goodman et al. 1995) find a constant P versus A_V trend, which in terms of P/A_V versus A_V will follow a steeply decreasing trend, indicating poor dust grain alignment at relatively higher opacities. Arce et al. (1998) have found a linear and flat trends in their P versus A_V for the stars lying behind the diffuse and dense regions of Taurus, respectively. However, their data in terms of P/A_V versus A_V , will follow similar trends that we observed in this work. Similarly, Jones et al. (2014) while studying the variation of fractional polarization per unit optical depth (P/τ) versus A_V towards a selection of starless cores using NIR and submm observations also find a change in the power-law from -0.5

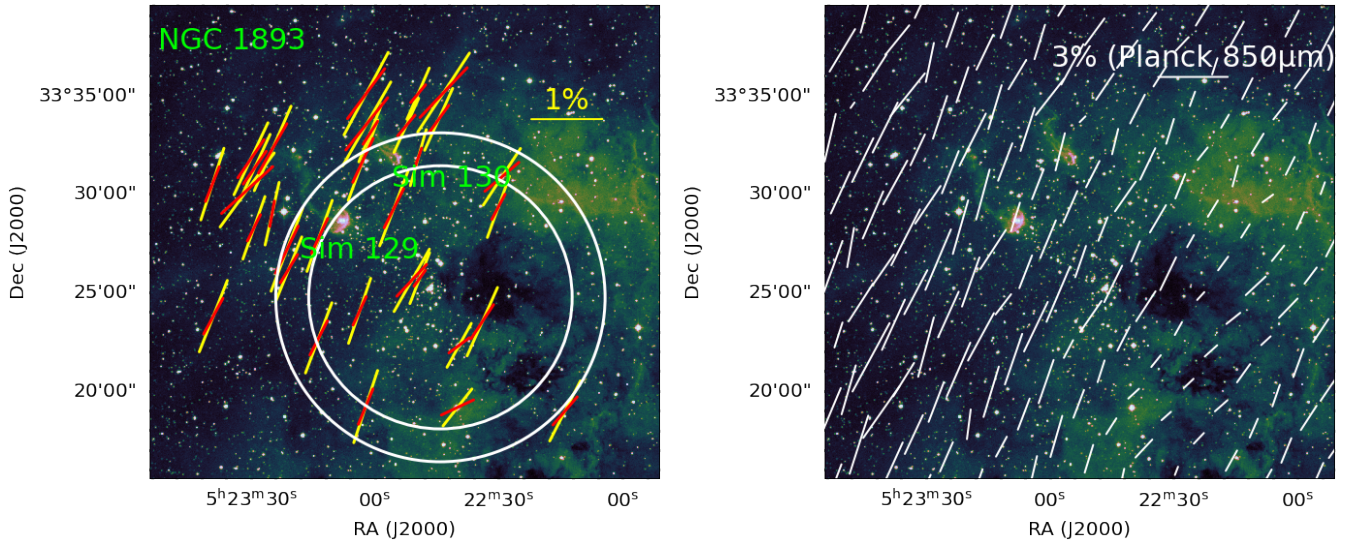


Figure 13. *Left:* Intrinsic magnetic field map of NGC 1893. The red coloured lines are the polarization vectors before the foreground subtraction, and the yellow coloured lines are the polarization vectors after the foreground subtraction. The length of the vector is proportional to the degree of polarization (P or P_{int}), whereas the orientation of the vector corresponds to the magnetic field orientation (PA or PA_{int}) with reference to equatorial north but increasing towards the east. Two concentric circles of radii $400''$ and $500''$ are shown. The region spanning between the two concentric circles denotes the $\sim 400'' - 500''$ region. The location of two emission nebulae Sim 129 and Sim 130 are also shown. *Right:* Oversampled (pixel size $1'$) magnetic field map morphology inferred based on *Planck*/353 GHz dust polarization data. The *Planck* magnetic field vectors (white) can be seen to match with those inferred from *I*-band polarization data presented in the left panel.

to -1 at $A_V \sim 20$ mag which is again similar to our trends. Another study carried out by Wang et al. (2017) showed that broken power-law prevails towards IC 5146 molecular cloud and evidenced a better dust grain alignment at relatively denser regions of the cloud with $A_V > 2.25$ mag in comparison to the poorly aligned dust grains in the low-density region with $A_V < 2.25$ mag. This result is in contrast to our result of efficiently aligned dust grains in the diffuse ISM and poorly aligned Perseus-arm dust.

From the broken power-law fit and Bayesian analysis of $d - P/d$ as presented in section 4.2, it is seen that the rate of polarization decreases steeply as a function of distance up to a threshold distance of ~ 2 kpc with a relation $P/d \propto d^{-0.8}$, thereafter P/d decreases but with a shallower rate with $P/d \propto d^{-0.3}$. We found that similar power-law indices have been found by the data on distance versus rate of extinction, d versus A_V/d plot as shown in Figure 15. The data up to ~ 2 kpc follow the relation $A_V/d \propto d^{-0.7}$, while beyond ~ 2 kpc they exhibit $A_V/d \propto d^{0.2}$. Therefore, the observed trends in the rate of extinction could be reflecting on the rate of polarization because both the quantities, extinction and polarization, are related. However, there exist a difference in the indices of the relations $P/d \propto d^{-0.3}$ and $A_V/d \propto d^{0.2}$ for stars with > 2 kpc. This implies that although the dust extinction increases abruptly beyond 2 kpc, the amount of polarization does not increase in the same proportion. We suggest that the rate of polarization plot reveals whether the dust grains are distributed in a uniform or non-uniform manner as a function of distance. To confirm this, we have plotted distance $_{i+1}$ versus differential extinction (ΔA_V) in Figure 16, which essentially reveals a constant and scattered distribution of ΔA_V corresponding to uniform and non-uniform dust distributions before and after 2 kpc, respectively.

Based on the analyses $A_V - P/A_V$, $d - P/d$, and the differential plots, we propose that there exist two dust populations: (i) the

foreground dust distributed between local Solar neighbourhood and Perseus arm and is – located up to ~ 2 kpc and characterized by $A_V < \sim 1$ mag, and (ii) the Perseus arm dust (Perseus-dust) could be part of the Perseus spiral arm in the direction of NGC 1893 and is – distributed beyond ~ 2 kpc and characterized by $A_V > \sim 1$ mag. Foreground dust is found to be uniformly distributed and efficiently aligned to the same degree at all distances to polarize the stellar light efficiently, as clear from the flat distribution in P/A_V versus A_V plot. In contrast, Perseus-dust seems to be non-uniform and not efficient enough to produce the polarization, as clear from the steeply decreasing trend in P/A_V versus A_V . Therefore, rate of polarization plot reveals about the distribution of dust, whereas the polarization efficiency plot sheds a light on dust grain alignment efficiency. We suggest that the observed differences in the polarization efficiency of the foreground and Perseus-dust are not due to the complex magnetic fields (but because of the differences in the dust distribution and their respective polarization efficiencies) as the magnetic field is found to be uniform across the entire line of sight to NGC 1893.

Although Perseus-dust seems to be non-uniform and poorly aligned, we assume that it infers the intra-cluster medium properties with a proper treatment of foreground subtraction and excluding stars with distance less than 3 kpc as well as lower SN ratio of intrinsic polarization (see Section 4.4). From Figure 14, we notice that T_d , and $P_{int}/A_{V_{int}}$ parameters tend to increase up to $\sim 400'' - 500''$ distance from the cluster centre, but the total dust extinction, $A_{V_{int}}$, decreases up to $\sim 400'' - 500''$ distance. P_{int} at the same time tends to follow a constant trend up to $\sim 500''$. But interestingly, the magnetic field orientation in the cluster region, as inferred by PA_{int} , is found to be nearly constant at all the radial distances. This implies that the increasing trend seen in $P_{int}/A_{V_{int}}$ is not because of spatial variation in $A_{V_{int}}$ and of a constant trend in PA_{int} . Instead, it is most likely caused by an increase in the high energy stellar radiation

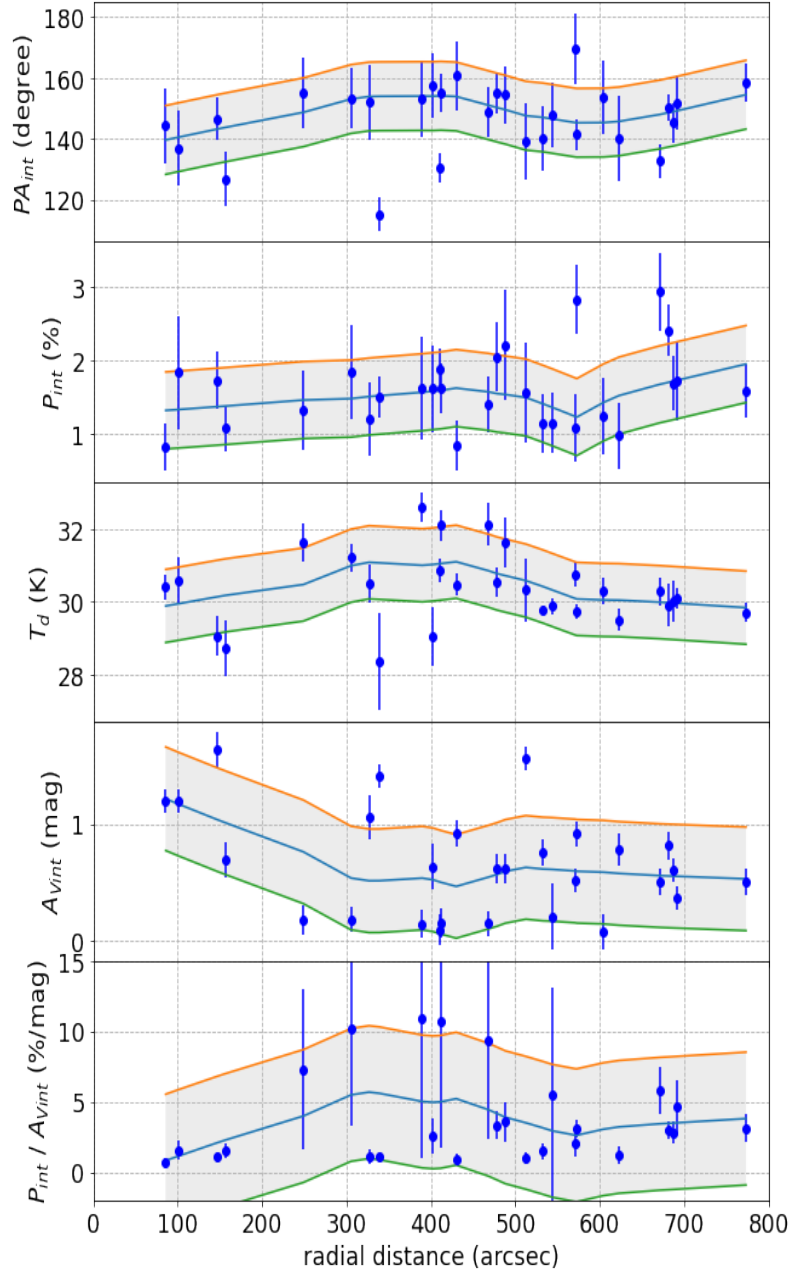


Figure 14. Variation of radial distance versus (a) PA_{int} , (b) P_{int} , (c) T_d , (d) A_{Vint} , and (e) P_{int}/A_{Vint} for the cluster members. The panels (a) – (d) consist of 28 stars, whereas panel (e) has 26 stars. Four stars which do not have reliable A_V values are removed from all the panels, and two additional stars with large errors in P_{int}/A_{Vint} are removed from panel (e). The overall trends traced by the LOWESS-smoothed curves (blue) are shown in all the panels. The corresponding $1-\sigma$ regions (grey) bounded by the $+\sigma$ (orange) and $-\sigma$ (green) lines are also shown.

emanating from the O/B type stars at the cluster center. Two emission nebulae Sim 129 and 130 are formed by the photoevaporation of the pre-existing clouds as a consequence of advancing ionization and shock fronts along with high energy UV photons and stellar winds originating from the O/B-type stars at the center of NGC 1893 cluster (see, Maheswar et al. 2007; Sharma et al. 2007). It is also possible that a number of newly formed pre-main-sequence stars around these nebulae could also act as secondary sources of radiation in the vicinity of Sim 129 and 130 so as to alter the dust grain alignment.

Such an increase in the amount of radiation towards the two nebulae can also increase the dust temperature T_d . This would result in

a better alignment of the dust grains in accordance with the RAT mechanism (Tram et al. 2021). Consequently, this in turn would be resulting in a higher polarization efficiency (P_{int}/A_{Vint}) towards the two nebulae. Therefore, increase in the amount of radiation could be the plausible reason behind the observed increase in the two parameters T_d , and P_{int}/A_{Vint} close to the two emission nebulae in the region distributed between $\sim 400'' - 500''$ as represented with two concentric circles in Figure 13 (Left).

We further performed a power-law fit to the T_d versus P_{int} data to quantify the existence of any positive correlation. As shown in Figure 17, the data exhibits a positive power-law index of 0.66 indicating

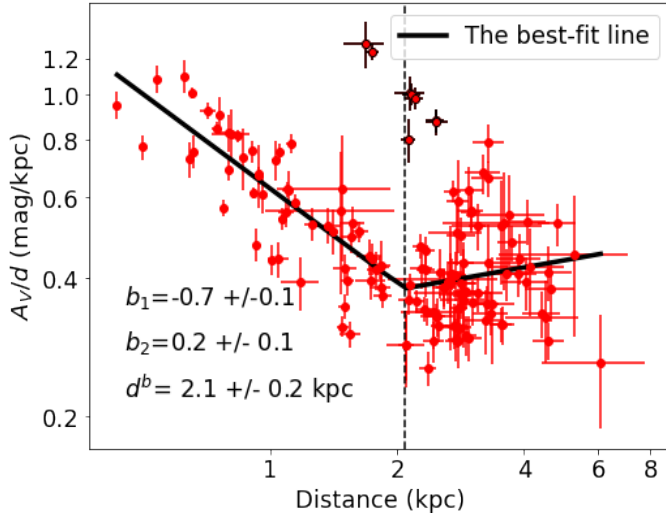


Figure 15. Distance versus A_V/d plot. The Best fit broken power-law is denoted with a thick line. The dotted vertical line corresponds to d^b at which the power-law breaks. Eight scattered points shown with black error bars are excluded while performing the fit. The Best-fit parameters are also overlaid.

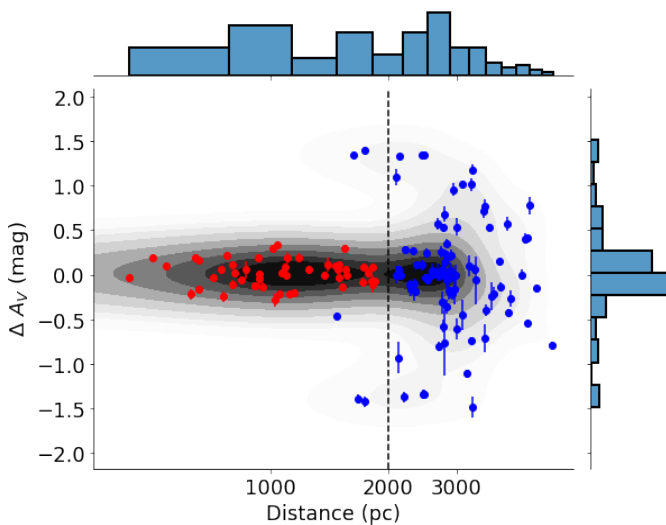


Figure 16. The differential density plot: distance versus ΔA_V . The darker background is corresponding to the higher probability density, whereas the lighter density for lower probability density. Two groups of stars: foreground stars (blue) and cluster members and background stars (red) identified by the GMM are overlaid. The vertical dotted line denotes 2 kpc where the transition is observed. The constant and scattered distributions of ΔA_V corresponds to the uniform and non-uniform dust distributions before and after 2 kpc, respectively. Two-dimensional histograms in each panel are also shown.

slow increase in P_{int} as a function of increase in T_d . To confirm this correlation, we perform the spearman rank-order correlation test using the *scipy-stats* module in PYTHON. The spearman test gives two outputs: correlation coefficient (r) and probability for an uncorrelated system of datasets (p-value), which are given to be 0.139 and 0.48, respectively. The small positive r -value and statistically insignificant p-value (as $p > 0.05$) indicates a very weak correlation between T_d and P_{int} .

Nevertheless, within a range, $\sim 29.5 - 31$ K, of T_d , the P_{int} is seen to exhibit a scattered distribution. Within this range of temperatures,

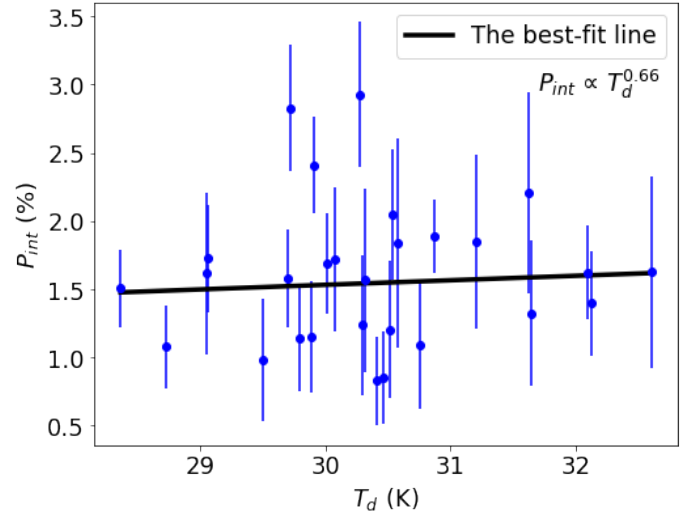


Figure 17. T_d versus P_{int} plot with the best fit power-law (thick line). The power-law relation is also overlaid.

some dust grains show relatively higher P_{int} values ($P_{int} > 2.3\%$) probably due to better alignment by RAT mechanism.

To confirm this, we have examined offset angle (ψ) between the magnetic field and the radiation field emanating from two O/B-type stars (HD 242935 and BD +33° 1025 that are located at the center of the NGC 1893 cluster) for three stars whose P_{int} values are higher than 2.3%. The ψ angles are found to be 63°, 80°, and 68° and in the order of increasing level of P_{int} . According to [Lazarian & Hoang \(2021\)](#), for $\psi > 45^\circ$ the fraction of dust grains driven to high J-atttractor points increase significantly due to weaker rotational disruption and relatively strong RAT, thereby resulting in a higher fraction of polarization (P_{int}). Therefore, three stars with $\psi > 45^\circ$ exhibit relatively higher P_{int} could be due to enhanced RAT mechanism.

6 SUMMARY AND CONCLUSIONS

The main aim of this paper is to investigate whether polarization observations from a distant target enable us to reveal the dust properties and magnetic field orientation within the target of interest. For this purpose, we have studied the variation of interstellar polarization as a function of extinction and distance towards the direction of NGC 1893. We have utilized the newly acquired *I*-band polarization data from ARIES IMaging POLarimeter (AIMPOL) plus the already published *I*-band polarization data ([Eswaraiah et al. 2011](#)). In addition, we also utilize distances from [Bailer-Jones et al. \(2021\)](#) and extinction data from [Green et al. \(2019\)](#). We have analysed two key plots (i) polarization efficiency (P/A_V) as a function of extinction (A_V) and (ii) rate of polarization (P/d) as a function of distance (d) by employing fitting (i) broken power-law and (ii) Bayesian analysis on both of the plots.

The following are the main conclusions of our study:

- The analyses on extinction (A_V) versus polarization efficiency (P/A_V) plot reveals a flat trend with a power-law index of ~ 0 up to the threshold extinction, A_V^b , of 1 mag. For $A_V > \sim 1$ mag, P/A_V exhibits a steeply decreasing trend with a power-law index ranging from -1.2 to -0.7 .

- The analyses on distance (d) versus rate of polarization (P/d) suggest that P/d declines steeply with an index of -0.8 up to the threshold distance, d^b , of ~ 1.5 kpc and beyond which the index is found to be -0.6 indicating same declining rate of polarization but with a lesser degree.

- Based on the analyses of $A_V - P/A_V$ and $d - P/d$, we suggest that there exist two dust populations: (1) foreground dust characterized by $A_V < \sim 1$ mag and distributed up to ~ 2 kpc distance, and (2) Perseus-arm dust (Perseus dust) characterized by $A_V > \sim 1$ mag and distributed beyond ~ 2 kpc.

- The relations $A_V - P/A_V$ and $d - P/d$ reveal two different clues about the dust grain properties: the former is about dust grain alignment efficiency and the latter is on the distribution of dust.

- We find that foreground dust is uniformly distributed and efficiently aligned, whereas the Perseus-dust is non-uniformly distributed and poorly aligned.

- After correcting for foreground polarization, we have derived the intrinsic polarization parameters (P_{int} and PA_{int}) and other parameters such as intrinsic extinction ($A_{V_{int}}$), dust temperature (T_d), and intrinsic polarization efficiency ($P_{int}/A_{V_{int}}$).

- The magnetic field orientation within the star forming region is found to be almost constant, and is not too different from that in the foreground medium.

- We notice an increasing trend in T_d , and $P_{int}/A_{V_{int}}$ towards the two nebulae Sim 129 and Sim 130, which we attribute to the increase in the stellar radiation emanating from the O/B-type stars located near the cluster centre of NGC 1893 or to the pre-main-sequence stars in the vicinity of the two nebulae which can act as secondary sources of radiation.

- T_d and P_{int} shows a very weak correlation, however a fewer data points show relatively higher polarization could be due to RAT mechanism.

In order to strengthen our statements, we plan to perform similar analyses using the polarization, extinction, and distance data towards other stellar clusters that are situated towards the direction of, but lying close to, NGC 1893.

ACKNOWLEDGEMENTS

We thank the referee for constructive suggestions which have improved the content and flow of this paper. C.E. acknowledges the financial support from grant RJF/2020/000071 as a part of Ramanujan Fellowship awarded by Science and Engineering Research Board (SERB), Department of Science and Technology (DST), Govt. of India. C.E. and B.N thank Prem Prakash and Belinda Damian for their help in programming and analyses. This work is done as part of the MS thesis project at Indian Institute of Science Education and Research (IISER) Tirupati.

DATA AVAILABILITY

The partial data is given in Table 1 and the complete dataset can be accessed online in the Harvard Dataverse using the following link: <https://dataverse.harvard.edu/privateurl.xhtml?token=76d51b62-b334-4289-aa3c-34a265634266>.

REFERENCES

- Amôres E. B., et al., 2021, *MNRAS*, **508**, 1788
- Andersson B., Potter S., 2005, *Monthly Notices of the Royal Astronomical Society*, **356**, 1088
- Andersson B., Pintado O., Potter S., Straižys V., Charcos-Llorens M., 2011, *Astronomy & Astrophysics*, **534**, A19
- Andersson B., Lazarian A., Vaillancourt J. E., 2015, *Annual Review of Astronomy and Astrophysics*, **53**, 501
- Arce H. G., Goodman A. A., Bastien P., Manset N., Sumner M., 1998, *The Astrophysical Journal Letters*, **499**, L93
- Bailer-Jones C. A. L., Rybizki J., Fouesneau M., Demleitner M., Andrae R., 2021, *VizieR Online Data Catalog*, p. I/352
- Baug T., et al., 2020, *ApJ*, **890**, 44
- Bessell M. S., Brett J. M., 1988, *PASP*, **100**, 1134
- Cantat-Gaudin T., et al., 2019, *Astronomy & Astrophysics*, **624**, A126
- Cardelli J. A., Clayton G. C., Mathis J. S., 1989, in Allamandola L. J., Tielens A. G. G. M., eds, Vol. 135, *Interstellar Dust*. pp 5–10
- Cashman L. R., Clemens D., 2014, *The Astrophysical Journal*, **793**, 126
- Chapman N. L., Goldsmith P. F., Pineda J. L., Clemens D., Li D., Krčo M., 2011, *The Astrophysical Journal*, **741**, 21
- Chen B., et al., 2019, *Monthly Notices of the Royal Astronomical Society*, **483**, 4277
- Cleveland W. S., 1979, *Journal of the American Statistical Association*, **74**, 829
- Cutri R. M., et al., 2003, *VizieR Online Data Catalog*, **2246**, 0
- Davis Jr L., Greenstein J. L., 1951, *The Astrophysical Journal*, **114**, 206
- Dolginov A., Mytrophanov I., 1976, *Astrophysics and Space Science*, **43**, 291
- Dougherty S. M., Waters L. B. F. M., Burki G., Cote J., Cramer N., van Kerkwijk M. H., Taylor A. R., 1994, *A&A*, **290**, 609
- Draine B. T., Weingartner J. C., 1996, *ApJ*, **470**, 551
- Draine B., Weingartner J. C., 1997, *The Astrophysical Journal*, **480**, 633
- Ducourant C., et al., 2017, *Astronomy & Astrophysics*, **597**, A90
- Eswaraiah C., Pandey A. K., Maheswar G., Medhi B. J., Pandey J. C., Ojha D. K., Chen W. P., 2011, *MNRAS*, **411**, 1418
- Eswaraiah C., Pandey A. K., Maheswar G., Chen W. P., Ojha D. K., Chandola H. C., 2012, *MNRAS*, **419**, 2587
- Eswaraiah C., Maheswar G., Pandey A. K., Jose J., Ramaprakash A. N., Bhatt H. C., 2013, *A&A*, **556**, A65
- Eswaraiah C., et al., 2019, *The Astrophysical Journal*, **875**, 64
- Franco G. A., Alves F. d. O., Girart J. M., 2010, *The Astrophysical Journal*, **723**, 146
- Gaze V., Shajn G., 1952, *Izvestiya Ordena Trudovogo Krasnogo Znameni Krymskoj Astrofizicheskij Observatorii*, **9**, 52
- Gerakines P., Whittet D., Lazarian A., 1995, *The Astrophysical Journal*, **455**, L171
- Goodman A. A., Jones T. J., Lada E. A., Myers P. C., 1992, *The Astrophysical Journal*, **399**, 108
- Goodman A. A., Jones T. J., Lada E. A., Myers P. C., 1995, *The Astrophysical Journal*, **448**, 748
- Green G. M., et al., 2015, *ApJ*, **810**, 25
- Green G. M., et al., 2018, *MNRAS*, **478**, 651
- Green G. M., Schlafly E., Zucker C., Speagle J. S., Finkbeiner D., 2019, *ApJ*, **887**, 93
- Hall J. S., 1949, *Science*, **109**, 166
- Heiles C., 2000, *AJ*, **119**, 923
- Hernández J., Calvet N., Hartmann L., Briceño C., Sicilia-Aguilar A., Berlind P., 2005, *AJ*, **129**, 856
- Hiltner W., 1949a, *The Astrophysical Journal*, **109**, 471
- Hiltner W., 1949b, *Science*, **109**, 165

- Jones T. J., Bagley M., Krejny M., Andersson B.-G., Bastien P., 2014, *The Astronomical Journal*, 149, 31
- Jones T. J., Bagley M., Krejny M., Andersson B. G., Bastien P., 2015, *AJ*, 149, 31
- Kharchenko N. V., Piskunov A. E., Röser S., Schilbach E., Scholz R. D., 2005, *A&A*, 440, 403
- Krone-Martins A., Soubiran C., Ducourant C., Teixeira R., Le Campion J., 2010, *Astronomy & Astrophysics*, 516, A3
- Kumar B., Pandey S., Eswaraiah C., Gorosabel J., 2014, *Monthly Notices of the Royal Astronomical Society*, 442, 2
- Kumar B., et al., 2019, *MNRAS*, 488, 3089
- Lazarian A., 2007, *Journal of Quantitative Spectroscopy and Radiative Transfer*, 106, 225
- Lazarian A., Hoang T., 2007, *MNRAS*, 378, 910
- Lazarian A., Hoang T., 2021, *ApJ*, 908, 12
- Lee H. M., Draine B. T., 1985, *ApJ*, 290, 211
- Lee C., Eswaraiah C., Chen W.-P., Pandey A., 2018, *The Astronomical Journal*, 156, 115
- Maheswar G., Sharma S., Biman J. M., Pandey A. K., Bhatt H. C., 2007, *MNRAS*, 379, 1237
- Marco A., Negueruela I., 2002, *A&A*, 393, 195
- Massey P., Johnson K. E., Degioia-Eastwood K., 1995, *ApJ*, 454, 151
- Melchior P., Goulding A. D., 2018, *Astronomy and computing*, 25, 183
- Meyer M. R., Calvet N., Hillenbrand L. A., 1997, *AJ*, 114, 288
- Pandey A. K., Samal M. R., Yadav R. K., Richichi A., Lata S., Pandey J. C., Ojha D. K., Chen W. P., 2014, *New Astron.*, 29, 18
- Pattle K., et al., 2019, *ApJ*, 880, 27
- Planck Collaboration et al., 2016a, *A&A*, 594, A1
- Planck Collaboration et al., 2016b, *A&A*, 594, A8
- Quinn J. L., 2012, *A&A*, 538, A65
- Rautela B. S., Joshi G. C., Pandey J. C., 2004, *Bulletin of the Astronomical Society of India*, 32, 159
- Rice S. O., 1945, *Bell System Technical Journal*, 24, 46
- Salvatier J., Wieckia T. V., Fonnesbeck C., 2016, *PyMC3: Python probabilistic programming framework* (ascl:1610.016)
- Savage B. D., Mathis J. S., 1979, *ARA&A*, 17, 73
- Schmidt G. D., Elston R., Lupie O. L., 1992, *AJ*, 104, 1563
- Schnee S. L., Ridge N. A., Goodman A. A., Li J. G., 2005, *ApJ*, 634, 442
- Serkowski K., Mathewson D. S., Ford V. L., 1975, *ApJ*, 196, 261
- Sharma S., Pandey A. K., Ojha D. K., Chen W. P., Ghosh S. K., Bhatt B. C., Maheswar G., Sagar R., 2007, *MNRAS*, 380, 1141
- Simmons J. F. L., Stewart B. G., 1985, *A&A*, 142, 100
- Tamura M., Nagata T., Sato S., Tanaka M., 1987, *Monthly Notices of the Royal Astronomical Society*, 224, 413
- Tram L. N., Hoang T., Lee H., Santos F. P., Soam A., Lesaffre P., Gusdorf A., Reach W. T., 2021, *ApJ*, 906, 115
- Van Leeuwen F., 2007, *A&A*, 474, 653
- Van de Schoot R., et al., 2021, *Nature Reviews Methods Primers*, 1, 1
- Wang J.-W., Lai S.-P., Eswaraiah C., Clemens D. P., Chen W.-P., Pandey A. K., 2017, *ApJ*, 849, 157
- Wang J.-W., et al., 2019, *ApJ*, 876, 42
- Wardle J. F. C., Kronberg P. P., 1974, *ApJ*, 194, 249
- Whittet D. C., 2018, *Dust in the galactic environment*. CRC press
- Whittet D., Hough J., Lazarian A., Hoang T., 2008, *The Astrophysical Journal*, 674, 304

APPENDIX A: BAYESIAN ANALYSES

Bayesian analysis is a method of statistical inference, where the available knowledge about parameters in a statistical model is updated with the information in the observed data. The background knowledge is expressed as a prior distribution and combined with observational data in the form of a likelihood function to determine the posterior distribution (Van de Schoot et al. 2021). The most general form of Bayesian inference is:

$$P(\theta/D) = \frac{P(\theta) \cdot P(D/\theta)}{P(D)} \quad (\text{A1})$$

$$\text{Posterior} = \frac{\text{Prior} \cdot \text{Likelihood}}{\text{Evidence}} \quad (\text{A2})$$

where D is the observed data and θ represents the model parameters. The posterior $P(\theta/D)$ describes the probability of the model parameters matching the given data. The evidence $P(D)$ is the probability of obtaining the data, which mainly serves as a normalization factor for the posterior. The prior $P(\theta)$ serves as the initial guessing probability of the model parameters based on our prior knowledge. The likelihood $P(D/\theta)$ describes how likely it is for a given model parameter set to match the observed data.

We already know from previous studies that the probability density function (PDF) of fractional polarization (P) follows a Rician distribution (Rice 1945; Wardle & Kronberg 1974; Simmons & Stewart 1985; Quinn 2012). Similarly, to determine the exact PDF distributions followed by P/A_V and P/d we use the *distfit* package in PYTHON. It compares the distributions of P/A_V and P/d with 26 continuous distributions available in *scipy-stats*, a module in python, to find the distribution which can fit the P/A_V and P/d data best. *distfit* ranks the 26 candidate distributions from best to worst based on their Residual Sum of Squares (RSS) values. As a result, the best fit distributions with the lowest values of RSS are selected. Hence, we find that P/A_V follow a Student's T distribution, and has PDF of the form:

$$f(x/x_0, \sigma, \nu) = \frac{\Gamma(\nu+1/2)}{\Gamma(\nu/2)} \left(\frac{\sigma}{\pi\nu}\right)^{1/2} \left(1 + \frac{\sigma(x-x_0)^2}{\nu}\right)^{-\frac{(\nu+1)}{2}} \quad (\text{A3})$$

where x and x_0 are the observed and real values of P/A_V , and σ is the uncertainty in any observed value of P/A_V . Γ is the gamma function, and ν is the degrees of freedom of the Student's T distribution. Similarly, P/d is found to follow a Rician distribution with the PDF given by:

$$g(x/x_0, \sigma) = \frac{x}{\sigma^2} \cdot \exp\left(-\frac{(x^2+x_0^2)}{2\sigma^2}\right) I_0\left(\frac{xx_0}{\sigma^2}\right), \quad (\text{A4})$$

where x and x_0 are the observed and real values of P/d and σ is the uncertainty in any observed value of P/d . I_0 is the zeroth order modified Bessel function. The likelihood functions L and L' , respectively for P/A_V and P/d , can be defined as:

$$L(x_0, \sigma, \nu) = \prod_{i=1}^{\infty} f(x_n/x_0, \sigma, \nu) \quad (\text{A5})$$

$$L'(x_0, \sigma) = \prod_{i=1}^{\infty} g(x_n/x_0, \sigma) \quad (\text{A6})$$

Here x_n represents the n^{th} measurement of P/A_V in equation A5 and P/d in equation A6 respectively. To perform the fit to the two plots using Bayesian method, we assume the following broken power-law model for $A_V - P/A_V$:

$$x_0 = \begin{cases} \alpha \cdot \left(\frac{z}{A_V^b}\right)^{\beta_1}, & \text{for } z \leq A_V^b \\ \alpha \cdot \left(\frac{z}{A_V^b}\right)^{\beta_2}, & \text{for } z > A_V^b \end{cases} \quad (\text{A7})$$

Here α , β_1 , and β_2 are the free model parameters. x_0 is the real value of P/A_V , z is A_V , and A_V^b is the A_V at which break occurs in $A_V - P/A_V$. Similarly, for $d - P/d$, we assume a broken power-law similar

to equation A7, where x_0 , A_V , and A_V^b are replaced with P/d , d and, d^b i.e, the d at which the break occurs in $d - P/d$ respectively.

For each relation, we define uniform priors within reasonable limits based on the best-fit parameters and their uncertainties from broken power laws (see Section 3.1 and Table 2).

The following are the priors:

(a) For $A_V - P/A_V$:

$$\begin{aligned}
 P(\alpha) &= \begin{cases} \text{uniform} & \text{if } 0 < \beta < 5 \\ 0 & \text{otherwise} \end{cases} \\
 P(\beta_1) &= \begin{cases} \text{uniform} & \text{if } -0.5 < \alpha_1 < 0.5 \\ 0 & \text{otherwise} \end{cases} \\
 P(\beta_2) &= \begin{cases} \text{uniform} & \text{if } -2 < \alpha_2 < -0.5 \\ 0 & \text{otherwise} \end{cases} \\
 P(A_V^b) &= \begin{cases} \text{uniform} & \text{if } 0.5 < A_V^b < 1.1 \\ 0 & \text{otherwise} \end{cases} \\
 P(\sigma) &= \begin{cases} \text{uniform} & \text{if } 0 < \sigma < 1.5 \\ 0 & \text{otherwise} \end{cases} \quad (\text{A8})
 \end{aligned}$$

(b) For $d - P/d$:

$$\begin{aligned}
 P(\alpha) &= \begin{cases} \text{uniform} & \text{if } 0 < \beta < 2 \\ 0 & \text{otherwise} \end{cases} \\
 P(\beta_1) &= \begin{cases} \text{uniform} & \text{if } -1.4 < \alpha_1 < 0 \\ 0 & \text{otherwise} \end{cases} \\
 P(\beta_2) &= \begin{cases} \text{uniform} & \text{if } -1 < \alpha_2 < 0 \\ 0 & \text{otherwise} \end{cases} \\
 P(d^b) &= \begin{cases} \text{uniform} & \text{if } 0.5 < d^b < 2.5 \\ 0 & \text{otherwise} \end{cases} \\
 P(\sigma) &= \begin{cases} \text{uniform} & \text{if } 0 < \sigma < 1 \\ 0 & \text{otherwise} \end{cases} \quad (\text{A9})
 \end{aligned}$$

For the above two plots, Bayesian modelling is performed using a Python package called PyMC3 (Salvatier et al. 2016) via Markov Chain Monte-Carlo (MCMC) method using the Metropolis-Hastings sampling algorithm. The 95%, 68%, and 50% confidence regions (CRs) predicted by the posterior distribution for each of the two plots are shown in Figure 5. From the figures, it is seen that the majority of the data fall well within 95% CR predicted by the posterior. The 94% highest density intervals (HDI) of each parameter are plotted to represent the data lying within 2σ uncertainties. The posterior PDF of the parameters derived from the Bayesian modelling is given in Figure 6. The parameters constrained through the Bayesian analyses are reasonably more accurate than those obtained from the broken power-law alone. The constrained results from Bayesian analyses are listed in Table 3.

To determine whether the broken power-law Bayesian model better represent the data over single-power-law Bayesian model, we perform the leave one out (*loo*) cross-validation using *ArviZ* module in PYTHON. *loo* cross validation estimates the expected log pointwise predictive density (elpd_{loo}) values for the broken-power law and single-power law bayesian models using the Pareto-smoothed importance sampling (PSIS) procedure. The standard error in elpd_{loo} and the effective number of parameters are also estimated for both models. *ArviZ* then compares the broken power-law and single power-law models based on the standard errors in elpd_{loo} values and ranks the

models from best to worst. For both $A_V - P/A_V$ and $d - P/d$, *ArviZ* ranked the broken power-law as a better model over the single power-law.

This paper has been typeset from a $\text{\TeX}/\text{\LaTeX}$ file prepared by the author.